

Energy Transfer Between Hot Protons and Electromagnetic Ion Cyclotron Waves in Compressional Pc5 Ultra-low Frequency Waves

著者	Kitamura N., Shoji M., Nakamura S., Kitahara M., Amano T., Omura Y., Hasegawa H., Boardsen S.A., Miyoshi Y., Katoh Y., Teramoto M., Saito Y., Yokota S., Hirahara M., Gershman D.J., Giles B.L., Russell C.T., Strangeway R.J., Ahmadi N., Lindqvist P.-A., Ergun R.E., Fuselier S.A., Burch J.L.
journal or publication title	Journal of Geophysical Research: Space Physics
volume	126
number	5
page range	e2020JA028912-1-e2020JA028912-25
year	2021-04-05
URL	http://hdl.handle.net/10228/00009049

doi: <https://doi.org/10.1029/2020JA028912>

JGR Space Physics

RESEARCH ARTICLE

10.1029/2020JA028912

Key Points:

- Electromagnetic ion cyclotron wave enhancements were detected in a compressional ultralow frequency (ULF) wave
- Troughs of magnetic field intensity of the ULF wave are preferential locations for the cyclotron resonant energy transfer
- Due to compressional ULF wave, regions of the cyclotron resonant energy transfer can be narrow in magnetic local time

Supporting Information:

Supporting Information may be found in the online version of this article.

Correspondence to:











N. Kitamura,
kitamura@eps.s.u-tokyo.ac.jp

Citation:

Kitamura, N., Shoji, M., Nakamura, S., Kitahara, M., Amano, T., Omura, Y., et al. (2021). Energy transfer between hot protons and electromagnetic ion cyclotron waves in compressional Pc5 ultra-low frequency waves. *Journal of Geophysical Research: Space Physics*, 126, e2020JA028912. <https://doi.org/10.1029/2020JA028912>

Received 5 NOV 2020
Accepted 25 MAR 2021

Energy Transfer Between Hot Protons and Electromagnetic Ion Cyclotron Waves in Compressional Pc5 Ultra-low Frequency Waves

N. Kitamura¹ , M. Shoji² , S. Nakamura² , M. Kitahara² , T. Amano¹ , Y. Omura³ , H. Hasegawa⁴ , S. A. Boardsen^{5,6} , Y. Miyoshi² , Y. Katoh⁷ , M. Teramoto⁸ , Y. Saito⁴ , S. Yokota⁹ , M. Hirahara² , D. J. Gershman⁸ , B. L. Giles⁵ , C. T. Russell¹⁰ , R. J. Strangeway¹⁰ , N. Ahmadi¹¹ , P.-A. Lindqvist¹² , R. E. Ergun¹¹ , S. A. Fuselier^{13,14} , and J. L. Burch¹³

¹Department of Earth and Planetary Science, Graduate School of Science, The University of Tokyo, Tokyo, Japan, ²Institute for Space-Earth Environmental Research, Nagoya University, Nagoya, Japan, ³Research Institute for Sustainable Humanosphere, Kyoto University, Uji, Japan, ⁴Institute of Space and Astronautical Science, Japan Aerospace Exploration Agency, Sagami-hara, Japan, ⁵NASA Goddard Space Flight Center, Greenbelt, MD, USA, ⁶Goddard Planetary Heliophysics Institute, University of Maryland, Baltimore County, MD, USA, ⁷Department of Geophysics, Graduate School of Science, Tohoku University, Sendai, Japan, ⁸Faculty of Engineering, Kyushu Institute of Technology, Fukuoka, Japan, ⁹Department of Earth and Space Science, Graduate School of Science, Osaka University, Toyonaka, Japan, ¹⁰Department of Earth Planetary, and Space Sciences, University of California, Los Angeles, CA, USA, ¹¹Laboratory for Atmospheric and Space Physics, University of Colorado, Boulder, CO, USA, ¹²Royal Institute of Technology, Stockholm, Sweden, ¹³Southwest Research Institute, San Antonio, TX, USA, ¹⁴Department of Physics and Astronomy, University of Texas at San Antonio, San Antonio, TX, USA

Abstract The Magnetospheric Multiscale (MMS) spacecraft observed many enhancements of electromagnetic ion cyclotron (EMIC) waves in an event in the late afternoon outer magnetosphere. These enhancements occurred mainly in the troughs of magnetic field intensity associated with a compressional ultralow frequency (ULF) wave. The ULF wave had a period of ~2–5 min (Pc5 frequency range) and was almost static in the plasma rest frame. The magnetic and ion pressures were in antiphase. They are consistent with mirror-mode type structures. We apply the Wave-Particle Interaction Analyzer method, which can quantitatively investigate the energy transfer between hot anisotropic protons and EMIC waves, to burst-mode data obtained by the four MMS spacecraft. The energy transfer near the cyclotron resonance velocity was identified in the vicinity of the center of troughs of magnetic field intensity, which corresponds to the maxima of ion pressure in the compressional ULF wave. This result is consistent with the idea that the EMIC wave generation is modulated by ULF waves, and preferential locations for the cyclotron resonant energy transfer are the troughs of magnetic field intensity. In these troughs, relatively low resonance velocity due to the lower magnetic field intensity and the enhanced hot proton flux likely contribute to the enhanced energy transfer from hot protons to the EMIC waves by cyclotron resonance. Due to the compressional ULF wave, regions of the cyclotron resonant energy transfer can be narrow (only a few times of the gyroradii of hot resonant protons) in magnetic local time.

1. Introduction

In the magnetosphere, plasma waves strongly affect the dynamics of charged particles. One of the waves is the electromagnetic ion cyclotron (EMIC) wave. This wave mode can exist at a frequency below the proton cyclotron frequency with a left-handed polarization (L-mode) (e.g., Cornwall, 1965; Kennel & Petschek, 1966). In the magnetosphere, EMIC waves are often generated in the vicinity of the magnetic equator (Loto'aniu et al., 2005) and the free energy source is a temperature anisotropy of hot protons (e.g., Cornwall, 1965; Fu et al., 2016; Gary et al., 2017; Kennel & Petschek, 1966; Kozyra et al., 1984; Ofman et al., 2017; Shoji & Omura, 2014). Usually, the growth rate has a maximum at the propagation direction parallel (or anti-parallel) to the background magnetic field. There are stop bands, the frequency ranges where the L-mode wave cannot exist, just above the cyclotron frequencies of ions, when the plasma is composed of multiple ion species (Kozyra et al., 1984). For example, in the case where the plasma contains protons, He⁺, and O⁺, there are three distinct frequency bands where EMIC waves can exist. The EMIC waves detected between

the cyclotron frequency of protons ($f_{c_{H^+}}$) and that of He^+ ($f_{c_{\text{He}^+}}$) is called the proton-band EMIC wave. The wave detected between the cyclotron frequency of O^+ ($f_{c_{\text{O}^+}}$) and $f_{c_{\text{He}^+}}$ is called the He-band EMIC wave. The wave detected below $f_{c_{\text{O}^+}}$ is called the O-band EMIC wave. The stop band just above $f_{c_{\text{He}^+}}$ is clearly seen in the statistical studies of EMIC waves observed by spacecraft in the magnetosphere (e.g., Fraser & Nguyen, 2001; Mauk et al., 1981; X.-J. Zhang et al., 2016).

The EMIC waves can scatter relativistic electrons by cyclotron resonance and can contribute to loss of the electron radiation belt (e.g., Denton et al., 2019; Kubota & Omura, 2017; Kurita et al., 2018; Lyons & Thorne, 1972; Miyoshi et al., 2008; Mourenas et al., 2016; Nakamura et al., 2019; Summers & Thorne, 2003; Thorne & Kennel, 1971). They can also heat heavy ions (e.g., Anderson & Fuselier, 1994; Berchem & Gen-drin, 1985; Fuselier & Anderson, 1996; Kitamura et al., 2018; Ma et al., 2019; Omura et al., 1985; Roux et al., 1982; Young et al., 1981; J.-C. Zhang et al., 2011). Because the EMIC wave scatters ions, it also contributes to the precipitation of protons to the atmosphere as proton aurora (e.g., Erlandson & Ukhorskiy, 2001; Miyoshi et al., 2008; Ozaki et al., 2018; Sakaguchi et al., 2008; Yahnina et al., 2000), and the precipitation of protons is one of the important decay mechanism of the ring current during geomagnetic storms (e.g., Cornwall et al., 1970; Jordanova et al., 2001; Kozyra et al., 1997). Because of such importance, global spatial distributions of EMIC waves have been extensively studied based on various in situ spacecraft observations (e.g., Allen et al., 2015; H. Chen et al., 2019; Jun et al., 2019; Keika et al., 2013; G.-J. Kim et al., 2016; Matsuda et al., 2018; Meredith et al., 2014; Min et al., 2012; Nakamura et al., 2016; Saikin et al., 2016; Usanova et al., 2012; X. Y. Wang et al., 2017). Some of the statistical studies include the data obtained in the outer magnetosphere (Allen et al., 2015; Keika et al., 2013; G.-J. Kim et al., 2016; Min et al., 2012; Usanova et al., 2012; X. Y. Wang et al., 2017), and they show that the EMIC waves are widely distributed on the day-side and have an occurrence peak in the afternoon sector.

Because these waves propagate away from the source region (Horne & Thorne, 1993), it is hard to prove that waves observed by a spacecraft are in the wave source region. This is one of the large difficulties in the study of electromagnetic waves. Recently the linear theory proxy (Blum et al., 2009; Gary et al., 1994) or the Kennel-Petschek anisotropy parameter (Noh et al., 2018) has been estimated and compared with observations of EMIC waves (Allen et al., 2016; R.-L. Lin et al., 2014; Noh et al., 2018; Saikin et al., 2018). Allen et al. (2016) showed that the linear theory proxy is preferable for the wave growth around the region where the occurrence of the EMIC waves is relatively high, while R.-L. Lin et al. (2014) stated the linear theory proxy cannot predict the occurrences of EMIC waves very well even in the vicinity of the equator. The linear theory proxy often also satisfies the criterion even when the EMIC waves were not observed (Noh et al., 2018; Saikin et al., 2018). The analysis based on the Kennel-Petschek anisotropy parameter implied that the proton distribution must often stay close to a marginal state (Noh et al., 2018). Thus, it has been difficult to discriminate the cases when the EMIC waves were and were not generated locally.

Attempts to detect energy transfer between charged particles and various waves or to detect the efficiency of pitch angle scattering of particles by waves have been reported and discussed (C. H. K. Chen et al., 2019; Ergun, Carlson, McFadden, Clemmons, Boehm, 1991; Ergun, Carlson, McFadden, TonThat et al., 1991; Fukuhara et al., 2009; Gershman, F-Viñas et al., 2017; He et al., 2019; Howes et al., 2017; Katoh et al., 2013, 2018; Kitahara & Katoh, 2016; Kitamura et al., 2018; Klein et al., 2017; Kletzing et al., 2005, 2017; T. C. Li et al., 2019; Shoji et al., 2017). Katoh et al. (2013) focused on the detection of the electron nongyrotropy that is caused by nonlinear wave-particle interactions between whistler mode waves and electrons (e.g., Omura et al., 2008) and tested the feasibility of such analysis in a simulation. The dot product between the resonant current and the wave component of the electric field is a key parameter for the energy transfer in the wave-particle interaction. The analysis method is called the wave-particle interaction analyzer (WPIA) (Fukuhara et al., 2009). Shoji et al. (2017) applied the WPIA method to data obtained by the Time History of Events and Macroscale Interactions during Substorms (THEMIS) spacecraft and detected a nongyrotropy of ions (called an ion hole), corresponding to the resonant current, which proved the energy transfer from ions to EMIC waves in the magnetosphere. Kitamura et al. (2018) identified the energy transfer rates between ions and EMIC waves at a temporal resolution of about one wave period. They took advantage of ion measurements from the Magnetospheric Multiscale (MMS) spacecraft with full sky field of view and very high temporal resolution (~ 80 measurements in one wave period). The WPIA method used in the present study is the same as that used by Kitamura et al. (2018) and is described in Section 2.

Modulation of one plasma wave mode by another wave mode is an interesting topic in studies of plasma waves. A clear example is the whistler mode waves modulated by compressional mirror mode waves, called lion roars, that are frequently observed in the magnetosheath (e.g., Ahmadi et al., 2018; Breuillard et al., 2018; Kitamura et al., 2020; Maksimovic et al., 2001; Smith et al., 1969; Smith & Tsurutani, 1976; Y. Zhang et al., 1998). Whistler mode waves are generated in the troughs of magnetic field intensity in the compressional mirror mode waves and cannot escape from the troughs, in cases where the amplitude of the compressional mirror mode waves is large (Kitamura et al., 2020). Thus, whistler mode waves are observed by a spacecraft only in the troughs of magnetic field intensity, and this condition causes very clear modulation (on-off) of whistler mode waves. Similar compressional waves, which are identified as ultralow frequency (ULF) waves around the frequency range of Pc 5 (period: 150–600 s), are often observed in the magnetosphere (e.g., Baumjohann et al., 1987; Constantinescu et al., 2009; Lanzerotti et al., 1969; Takahashi, Lopez et al., 1987; X. Zhu & Kivelson, 1994), and some of them include whistler mode waves only in the vicinity of the troughs of magnetic field intensity (Baumjohann et al., 2000; Dubinin et al., 2007; W. Li et al., 2011; Xia et al., 2016; X.-J. Zhang, Angelopoulos et al., 2020; X.-J. Zhang, Chen et al., 2019). On the other hand, the effect of ULF waves on EMIC waves is less understood, although the generation process of the whistler mode wave and the EMIC wave have much in common, except for the energy source: anisotropic electrons and ions, respectively. Events where the EMIC waves were likely modulated by a Pc 5 ULF wave were found and analyzed by Barfield and Coleman (1970) and Barfield and McPherron (1972). Large magnitude Poynting fluxes of EMIC waves were detected in the vicinity of the troughs of the magnetic field intensity (compressional component) of the ULF wave. This modulation is the same as that of lion roars. Although there are some studies of EMIC waves in ULF waves that followed these studies, most of the later studies focused on the toroidal mode of ULF waves (Mursula et al., 2001; Rasinkangas et al., 1994) or could not investigate the wave modes of ULF waves in space because only ground-based observations were available (Kakad et al., 2019; Plyasova-Bakounina et al., 1996; Rasinkangas & Mursula, 1998). Using the magnetic field and electric field data obtained by the Combined Release and Radiation Effects Satellite, Loto'aniu et al. (2009) found events with modulations of EMIC waves in compressional ULF waves similar to the example studied by Barfield and Coleman (1970) and Barfield and McPherron (1972). A decrease in Alfvén velocity and the cyclotron resonance energy due to the compressional ULF wave is suggested as the cause of the modulation, while a lack of particle measurements made it difficult to discuss the detailed feature of modulation of ions, for example, the temperature anisotropy. Loto'aniu et al. (2009) also found time intervals during which the EMIC wave appeared near the peaks of magnetic field intensity, contrary to the modulation discussed above. S. Liu et al. (2019) reported an event of modulations of EMIC waves in a ULF wave with a large compressional component. The EMIC waves were detected near the troughs of the magnetic field intensity, and the authors suggested that a fast mode wave, which was generated by quasiperiodic solar wind proton dynamic pressure enhancements observed in the interplanetary medium, was the cause of the ULF wave, while limited temporal resolution of the in-situ ion data (70 s) made it difficult to investigate the modulation of ions in the ULF wave in detail. Although X.-J. Zhang, Mourenas et al. (2019) also studied the EMIC waves in compressional ULF waves in the inner magnetosphere, no clear modulation was found. Thus, the detailed feature of modulations of EMIC waves and ions in compressional ULF waves is not well understood.

Statistical studies by X. Zhu & Kivelson (1991) and Nishi et al. (2018) showed that many magnetospheric compressional ULF waves have an antiphase relation between the magnetic and ion pressures. Based on event studies, such compressional ULF waves in the magnetosphere are thought to be generated by the drift mirror instability in many cases because of the antiphase relation and/or their small phase velocities in the plasma rest frame (e.g., Baumjohann et al., 1987; Constantinescu et al., 2009; Korotova et al., 2009; Lanzerotti et al., 1969; Rae et al., 2007; Soto-Chavez et al., 2019; Takahashi, Lopez et al., 1987; Vaivads et al., 2001; X. Zhu & Kivelson, 1994). The condition of the mirror instability is

$$\frac{T_{i_perp}}{T_{i_para}} - 1 - \frac{1}{\beta_{i_perp}} > 0, \quad (1)$$

where T_{i_perp} and T_{i_para} are the ion temperatures perpendicular and parallel to the magnetic field, respectively, and β_{i_perp} is the ratio of the perpendicular ion pressure to the magnetic pressure (Hasegawa, 1969). As shown in Equation 1, the ion temperature anisotropy ($T_{i_perp} > T_{i_para}$) is necessary for the mirror instability.

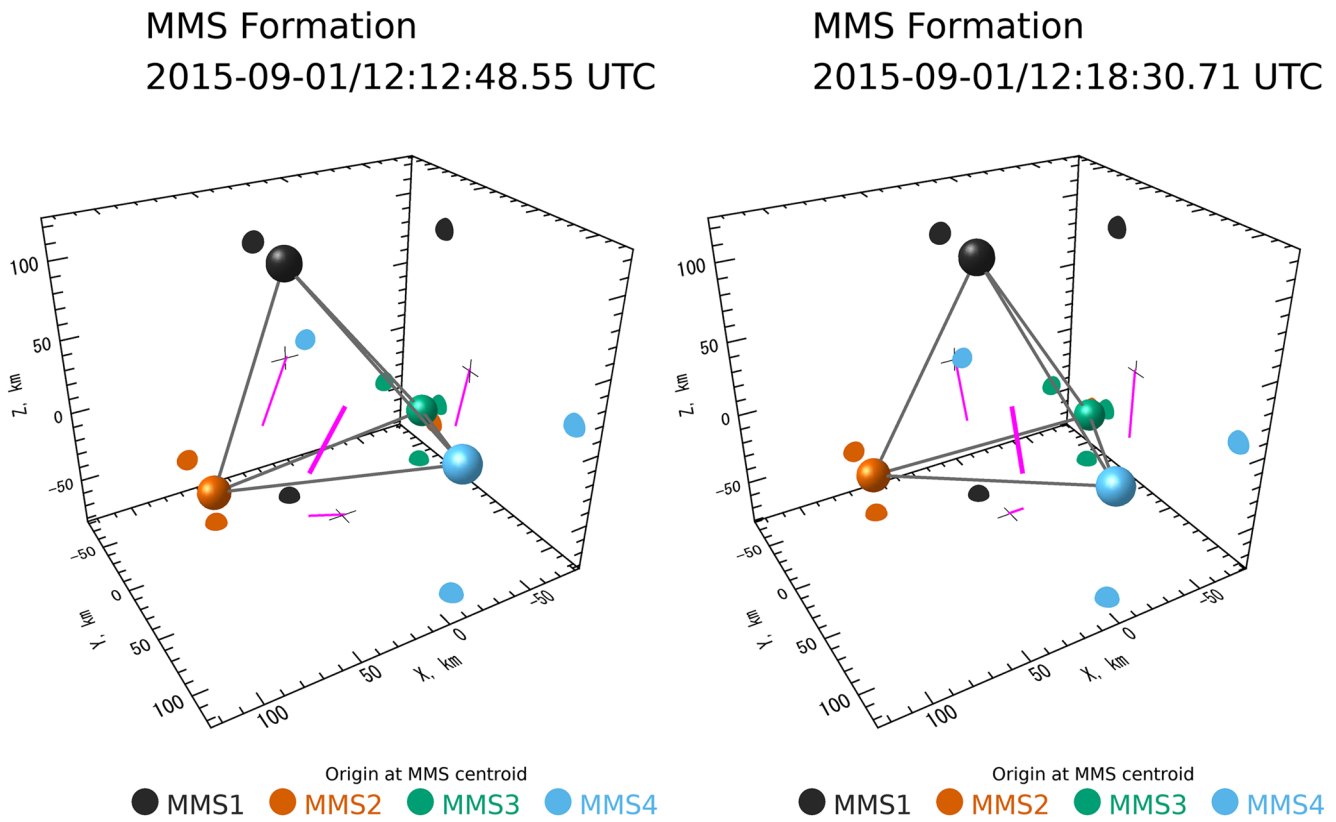


Figure 1. Formation of the MMS spacecraft in the field-aligned coordinates during EMIC wave events, where the burst data are available. (a) Event 1, and (b) Event 2. Magenta bars indicate the wave normal directions. EMIC, electromagnetic ion cyclotron; MMS, Magnetospheric Multiscale.

This anisotropy is the same as that for the cyclotron instability to generate EMIC waves. Thus, the co-existence of mirror mode structures and EMIC waves itself has been a subject of many studies (Ahmadi et al., 2016; Gary, 1992; Hubert et al., 1998; Shoji et al., 2009).

In the present study, using data obtained by the four MMS spacecraft (Burch et al., 2016), we investigate the propagation properties of ULF waves and EMIC waves observed in a ULF wave event in the late afternoon magnetosphere. Furthermore, we demonstrate an energy transfer from hot resonant anisotropic protons to EMIC waves, which is a strong indicator of the wave growth. We show that the observed ULF wave is almost a static structure in the plasma rest frame. Thus, we estimate the spatial extent of the EMIC wave and the region of the energy transfer in the ULF wave (or the magnetic field structure).

2. Geomagnetic Conditions, MMS Spacecraft and Data set

The event in this study was observed near the beginning of the first orbit of Phase-1a (September 1, 2015) of the MMS mission. The apogee of MMS in Phase-1a, which focused on the dayside magnetopause region, was ~ 12 Earth Radii (R_E). The spacecraft separation on September 1, 2015 was ~ 160 km ($\sim 0.025 R_E$) (Figure 1) (Fuselier et al., 2016). This scale is much smaller than the wavelengths of ULF and EMIC waves and the gyro-radius of hot protons (10–30 keV) as discussed in Appendices A and B. Thus, data are averaged over all four MMS spacecraft unless otherwise noted.

Using data from the fluxgate magnetometers (FGM) (Russell et al., 2016), we determined the background magnetic field (\mathbf{B}_{0_ULF} and \mathbf{B}_{0_EMIC}), wave magnetic field (\mathbf{B}_{w_ULF} and \mathbf{B}_{w_EMIC}), magnetic field intensity (B_0), and ion cyclotron frequencies ($f_{ci} = \Omega_{ci}/2\pi = qB_0/(2\pi m_i)$), where q and m_i are the charge and mass of ions, respectively. In the time interval shown, the sampling rate of FGM was 16 samples/s (fast survey). A fast Fourier transform (FFT) is applied to the FGM data to isolate the component of ULF and EMIC waves. To create waveform data (\mathbf{B}_{w_ULF} and \mathbf{B}_{w_EMIC}), an inverse FFT is applied to the Fourier-transformed

components of the FGM data between 0.001 and 0.05 Hz (period: 20–1,000 s) and between 0.05 and 0.15 Hz (period: 6.67–20 s), respectively. The same method (a combination of FFT and inverse FFT) is also used for frequency filtering hereafter. The low-pass filtered components below 0.001 and 0.05 Hz are derived for the background magnetic field data (\mathbf{B}_{0_ULF} and \mathbf{B}_{0_EMIC} , respectively), and they are used to define the field-aligned coordinates (FAC) for the analysis of ULF and EMIC waves. For the analysis of ULF (EMIC) waves, the intervals of 10:30:00–12:46:32 (12:11:14–12:15:30 and 12:15:28–12:24:00) UT on September 1, 2015 were used for this filtering. The $+z$ -direction of FAC corresponds to the direction of the background magnetic field. The $+x$ -direction is defined as the cross product of the geographically eastward vector and the $+z$ -direction. Thus, the x -direction is close to the radially outward direction. The remaining direction (y) is defined to complete an orthogonal right-handed coordinate system, and is close to the azimuthally eastward direction.

Only the component below 0.05 Hz (\mathbf{E}_0) of fast survey electric field data from the double probes (EDP) (Ergun et al., 2016; Lindqvist et al., 2016; Torbert et al., 2016) with a sampling rate of 32 samples/s were used to derive the $\mathbf{E} \times \mathbf{B}$ drift velocity of the background plasma in Appendix A. As described in supplemental material of Kitamura et al. (2018), EDP data could not be used to analyze the EMIC wave electric field in the present case (wave frequency, $f_{w_EMIC} \sim 0.1$ Hz), because there was a fluctuation with an amplitude comparable to the EMIC wave electric field around a frequency of ~ 0.1 Hz (half of the spin period) that was likely caused by ion beams from the Active Spacecraft Potential Control (ASPOC) neutralizers (Torkar et al., 2016). Because f_{w_EMIC} was much lower than f_{c_H+} in the events analyzed, perpendicular EMIC wave electric fields (\mathbf{E}_{w_EMIC}) were estimated from the cross product of the magnetic field and the cold ion velocity (\mathbf{v}_{i_cold}), calculated as a moment of distribution functions of ions observed by the Fast Plasma Investigations (FPI)-Dual Ion Spectrometer (DIS) (Pollock et al., 2016), with a correction because of the non-zero frequency. The ions in the energy range of 10–257 eV are used for the moment calculations of \mathbf{v}_{i_cold} . Kitamura et al. (2018) described a more detailed explanation in their supplemental material.

We use data from FPI-DIS, which has a full-sky field of view with temporal resolutions of 0.15 and 4.5 s in the burst and fast survey modes, respectively. The angular resolution is 11.25° . In Phase-1a, DIS covered the energy from 10 eV to 30 keV. Because wave observations in the magnetosphere are not the main target of the MMS mission, burst data exist only in a very limited part (two EMIC wave events in troughs of \mathbf{B}_{0_ULF}) of the time interval of the ULF waves. We analyzed energy transfer from hot protons to EMIC waves in detail for the two EMIC wave events using burst mode data. Fast survey data are mainly used for the analysis related to the ULF waves. To determine \mathbf{v}_{i_cold} for the analysis related to the ULF waves, fluctuations above 0.05 Hz were removed from \mathbf{v}_{i_cold} . Fast survey data (temporal resolution: 4.5 s) from FPI Dual Electron Spectrometer (DES) (Pollock et al., 2016), which cover the energy range from 10 eV to 30 keV, are additionally used mainly for calculations of plasma pressure. Although the upper limit of the energy range is 30 keV, the contribution from the population with energies >30 keV is taken into account for the moments in the Level-2 data by extrapolation as described by Pollock et al. (2016). Internal photoelectrons are subtracted from DES data (Gershman, Avananov et al., 2017).

We derive the energy transfer rate (perpendicular to \mathbf{B}_{0_EMIC}) using the WPIA method (e.g., Fukuhara et al., 2009; Katoh et al., 2013, 2018; Kitamura et al., 2018; Shoji et al., 2017). The energy transfer rate between ions and waves is calculated as the dot product of \mathbf{E}_{w_EMIC} and ion current (\mathbf{j}). Negative $\mathbf{j} \cdot \mathbf{E}$ indicates that the wave is gaining energy from ions (wave growth). We derived $\mathbf{j} \cdot \mathbf{E}_{w_EMIC}$ in various ranges of energy (~ 11 –30 keV) and pitch angles (33.75° – 146.25°) using the same method as Kitamura et al. (2018). To reduce the effect of the diamagnetic current associated with the large gradient of ion pressure in a compressional ULF wave, which does not rotate with \mathbf{E}_{w_EMIC} and sometimes causes large fluctuations of $\mathbf{j} \cdot \mathbf{E}_{w_EMIC}$, 15-s (\sim one wave period of the EMIC wave) moving averaged $\mathbf{j} \cdot \mathbf{E}_{w_EMIC}$ was used (Kitamura et al., 2018). Because a detailed analysis of the distribution function was performed by Kitamura et al. (2018) for one of the events, we focus on the observed temporal variation of $\mathbf{j} \cdot \mathbf{E}_{w_EMIC}$ in the present manuscript.

FPI-DIS sampled odd energy steps (32 steps), called parity 0, in the first half of each 0.3 s interval, and sampled even energy steps (parity 1) in the second half during Phase-1a. This sampling causes a change of the energy range and a fluctuation of \mathbf{j} with a period of 0.3 s when data in both parties are used. Nevertheless, because only the 15-s moving averaged $\mathbf{j} \cdot \mathbf{E}_{w_EMIC}$ is used as discussed above, the effect of the fluctuation is smoothed out. The energy ranges shown in the titles of figure panels are the average of those of parity 0

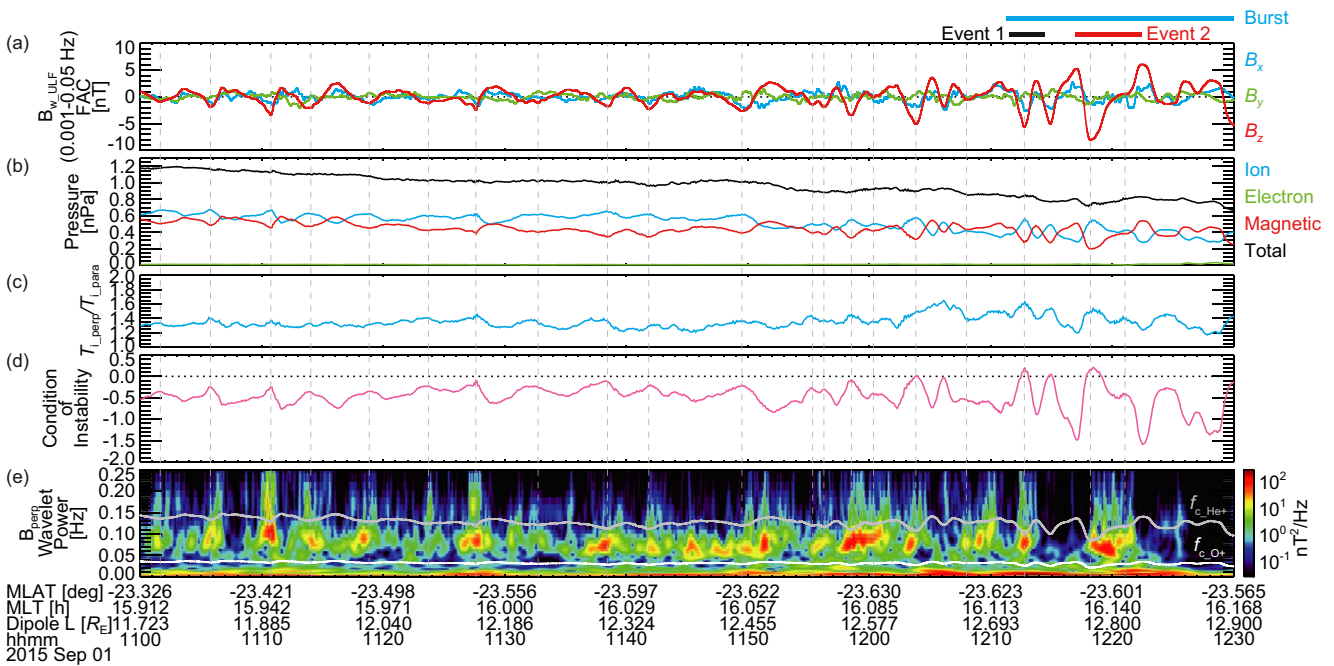


Figure 2. Overview of the EMIC waves and plasma data in the ULF wave. (a) Wave components of the magnetic field in the frequency range of 0.001–0.05 Hz (\mathbf{B}_{w_ULF}), (b) plasma (ion and electron) and magnetic pressures, (c) ion temperature ratio (T_{i_perp}/T_{i_para}), (d) the condition of the mirror instability, and (e) wavelet power spectrum of magnetic fields in the perpendicular (x-y in FAC) plane with cyclotron frequencies of He^+ ($f_{c_He^+}$, gray curve) and O^+ ($f_{c_O^+}$, white curve). Fast survey data are used for this plot. The period when the burst data are available is indicated by a blue bar above this plot. The intervals shown in Figure 3 (Event 1) and 4 (Event 2) are indicated by black and red bars, respectively, above the panels. Vertical dashed lines indicate the minima of $B_{w_ULF_z}$ when enhancements of EMIC waves were detected around the minima. EMIC, electromagnetic ion cyclotron; FAC, field-aligned coordinates; ULF, ultralow frequency.

and parity 1. In the case where we calculate $\mathbf{j} \cdot \mathbf{E}_{w_EMIC}$ using the data from all four spacecraft, \mathbf{j} and \mathbf{E}_{w_EMIC} were averaged separately, and then the dot product between them was calculated.

We verified that the FPI-DES burst mode data used in this study are not lossy compressed before the downlink (see Barrie et al., 2017, 2019 about lossy compression of the FPI data). Although the temporal resolution of the fast survey data obtained by FPI is higher than the wave period of the EMIC wave, as shown in the next section, the fast survey data always has high lossy compression (Barrie et al., 2017). Furthermore, because the fast survey data of FPI-DIS is the average of a series of 30 burst data points, breaking down to higher resolution data, as performed by Shoji et al. (2017) for the ion data obtained by the THEMIS spacecraft, is impossible. Thus, the burst data are necessary for the analysis of energy transfer on the basis of the WPIA method.

Fast survey data from the Hot Plasma Composition Analyzer (HPCA) (Young et al., 2016), which measures protons, He^{++} , He^+ , and O^+ in the energy range of ~ 1 eV–40 keV at a temporal resolution of 10 s, are used to confirm that protons were the dominant ion species ($>95\%$). Because the $\mathbf{E} \times \mathbf{B}$ drift velocity was ~ 30 km/s (Appendix A), even cold He^+ and O^+ with zero velocity in the plasma rest frame must have energies of ~ 19 and 75 eV, respectively, in the frame of the spacecraft and these energies are within the energy range of HPCA when ASPOC is on (spacecraft potential ~ 4 V).

3. Results

3.1. Overview of ULF and EMIC Waves

The ULF waves were observed from $\sim 10:30$ UT to at least 13:30 UT on September 1, 2015. During the period shown in Figure 2 (11:00–12:30 UT), MMS spacecraft traversed the late afternoon outer magnetosphere at the magnetic local time (MLT) from 15.9 to 16.2 h, the magnetic latitude (MLAT) from -23.3° to -23.6° ,

and dipole- L value from 11.7 to 12.9. This magnetic latitude is calculated as the angle from the $z = 0$ plane in the solar magnetic coordinate.

The geomagnetic activity and the solar wind conditions were quiet. The AL and $SYM-H$ indices were > -154 nT and -7 to -3 nT, respectively. The Kp index was 1+ (09:00–12:00 UT) and 1 (12:00–15:00 UT). After August 30, 2015, which was in the recovery phase of a geomagnetic storm that had multiple minima of the $SYM-H$ index around August 27–28, 2015, the Kp index was 2– or smaller. The time-shifted solar wind (OMNI 5-min) data between 11:00 and 12:30 UT indicate that the y and z components of interplanetary magnetic fields in Geocentric Solar Magnetospheric (GSM) coordinates stayed in the ranges from -4.20 to 0.64 and from -2.21 to 1.06 nT, respectively. The solar wind dynamic pressure was ~ 1.2 nPa (1.12 – 1.31 nPa) without large pressure pulses, although many EMIC wave events related to enhancements of solar wind dynamic pressure have been reported (e.g., Cho et al., 2016; Cho et al., 2017; Engebretson et al., 2018; K. H. Kim et al., 2017).

The MMS spacecraft encountered a density enhancement (Appendix C) until $\sim 12:21$ UT, interpreted to be a plasmaspheric plume. Upon exiting the plume at $\sim 12:21$ UT a strong enhancement is observed in the differential electron energy flux (Figure S1a) at energies higher than ~ 200 eV. Ions fluxes (Figure S1b) are observed with energies higher than ~ 1 keV that do not show clear changes, except for semi-periodic fluctuations related to the ULF wave that is discussed in detail later. The plume exit was likely the boundary between the region of eastward drifting hot electrons originally injected from the nightside and the inner region of high-density cold plasma, where injected hot electrons cannot penetrate.

The ULF wave periods were about 2–5 min, which is in the Pc5 frequency range (Figure 2a and Figure S1c). Because the velocity of propagation is estimated as ~ 30 km/s (westward) (Appendix A), the wavelength is estimated as $\sim 3,600$ – $9,000$ km that corresponds to the azimuthal wave number m from ~ -55 to -140 . The feature of the ULF waves at 10:30–11:00 UT (not shown) was similar to that at 11:00–11:30 UT. The fluctuation of $\mathbf{B}_{w,ULF}$ (0.001–0.05 Hz) was largest in the compressional component (z component in FAC), especially after $\sim 11:50$ UT (Figure 2a). The plasma (ion + electron) pressure was dominated by ions, and the fluctuations of the magnetic and ion pressures were in antiphase, such that the total pressure remained almost constant (Figure 2b). The plasma β , the ratio of the plasma pressure to the magnetic pressure, was close to 1, except for some large troughs of magnetic field intensity ($\beta \sim 2$ – 3) (Figure S1d). Hot ion fluxes at 14–30 keV had a peak around the pitch angle of 90° (Figure S1e), and thus perpendicular β is larger than parallel β . In many cases, the ion temperature ratio ($T_{i,perp}/T_{i,para}$) had a peak in a trough of magnetic field intensity (Figure 2c). These characteristics are consistent with the idea that the compressional fluctuations are generated by the mirror mode type instability (e.g., Hasegawa, 1969). Nevertheless, the condition of the mirror instability (Equation 1) was satisfied only at the center of some of the troughs (Figure 2d). This will be discussed in Section 4.3. Interestingly, butterfly type pitch angle distributions of ions, which have been predicted and observed in mirror structures (Kivelson & Southwood, 1996; Soucek & Escoubet, 2011), were identified around 2 keV in Event 1 (Figure S2a) and around 3 keV in Event 2 (Figure S2b).

Rae et al. (2007) and X. Zhu & Kivelson (1991) indicate that such compressional fluctuations are confined in the vicinity of the magnetic equator (= minimum of magnetic field intensity along field lines here). This confinement is consistent with the estimation by Kitamura et al. (2018) that the location of the MMS spacecraft was close ($\sim 1.5 R_E$) to the minimum of magnetic field intensity (minimum- B).

Many enhancements of He-band EMIC waves (below f_{c,He^+}) were detected in the vicinity of the troughs of the magnetic field intensity (Figure 2e), although the one-to-one correspondence is less clear than in the cases of whistler-mode waves observed in compressional waves (Baumjohann et al., 2000; Dubinin et al., 2007; W. Li et al., 2011; Xia et al., 2016; X.-J. Zhang, Angelopoulos et al., 2020; X.-J. Zhang, Chen et al., 2019). This point is discussed in Section 4.2. In some cases, weaker proton-band EMIC waves (between proton cyclotron frequency (f_{c,H^+} and f_{c,He^+}) were observed simultaneously with He-band EMIC waves. Burst data are available only during the last two enhancements (Event 1 and Event 2) of He-band EMIC waves, for which detailed analyses are performed in the next section.

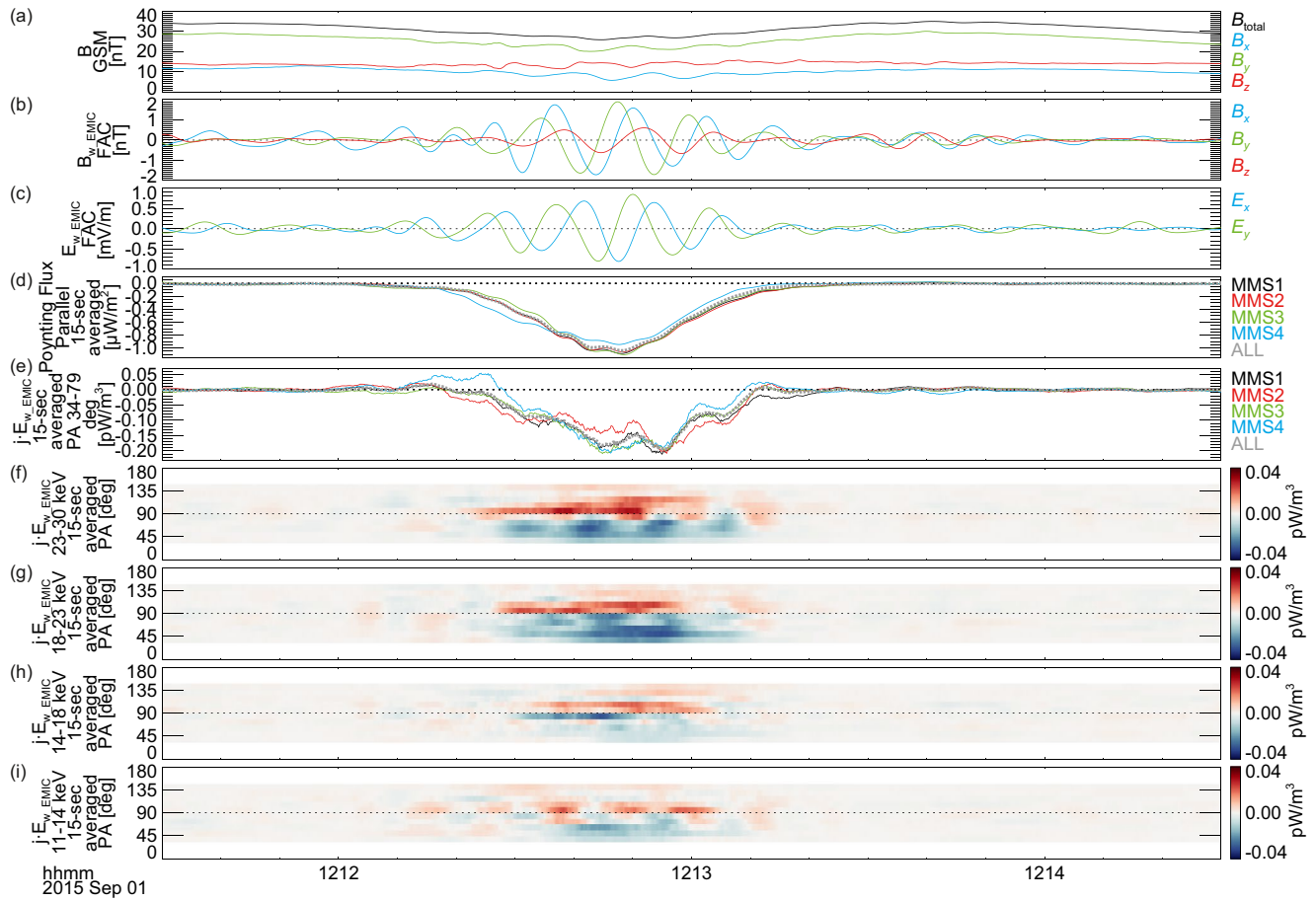


Figure 3. The detailed characteristics of the EMIC wave (Event 1). (a) The magnetic field from FGM in the GSM coordinates, (b) wave components of the magnetic field in the frequency range of 0.05–0.15 Hz (\mathbf{B}_{w_EMIC}), (c) wave components of the estimated electric field in the frequency range of 0.05–0.15 Hz (\mathbf{E}_{w_EMIC}), (d) 15-s moving averaged Poynting flux parallel to \mathbf{B}_{0_EMIC} , (e) 15-s moving averaged $\mathbf{j} \cdot \mathbf{E}_{w_EMIC}$ (ions in the pitch angle (PA) range of 33.75°–78.75° with energies of 14–30 keV), and (f–i) pitch angle spectra of $\mathbf{j} \cdot \mathbf{E}_{w_EMIC}$ in the energy ranges of 23–30, 18–23, 14–18, and 11–14 keV. EMIC, electromagnetic ion cyclotron; FGM, fluxgate magnetometers; GSM, Geocentric Solar Magnetospheric.

3.2. Energy Transfer Between Hot Protons and EMIC Waves

The trough of magnetic field intensity in the vicinity of Event 1 was a relatively small structure because the period of $B_{w_ULF_Z}$ was short compared with other troughs (Figure 2a). An enhancement of EMIC waves was observed in the vicinity of the center of the trough (Figures 3a–3c). Because the field-aligned component of the Poynting flux was negative (Figure 3d), the EMIC wave propagated southward (anti-parallel to \mathbf{B}_{0_EMIC}). Because the z (field-aligned) component of $\text{grad } B_{0_EMIC}$ was continuously negative (Figure S1g), the EMIC wave came from the region where the magnetic field intensity was smaller. Thus, the wave generation would start in the vicinity of minimum- B along the field line and the generated wave propagated toward the polar region. Although sometimes minimum- B points can exist at mid-latitude in the outer part of the magnetosphere (mainly in the dayside) and EMIC waves can be generated there (Allen et al., 2013; J. H. Lee et al., 2019; Y. H. Liu et al., 2012; Vines et al., 2019), the model magnetic fields (Thébault et al., 2015; Tsyganenko & Stern, 1996) suggest that this was not the case here, as described by Kitamura et al. (2018) in their Supplemental Material. The model magnetic field intensity at the location of the spacecraft is $\sim 8\%$ larger than that at the minimum- B .

Because the EMIC wave propagated anti-parallel to the magnetic field, the cyclotron resonance velocity became positive and some of the ions with pitch angle $< 90^\circ$ can resonate. For the background magnetic field intensity of 26 nT and the wave frequency (f_{EMIC}) of 0.0769 Hz as observed, the parallel components of the phase velocity (V_{ph_para}) and the cyclotron resonance velocity (V_{res}) were calculated as ~ -330 and

$\sim 1,370$ km/s, respectively (Appendix B). In the energy range of 18–30 keV, this V_{res} corresponds to the pitch angle of 42° – 55° (Figure S2a). Negative $\mathbf{j} \cdot \mathbf{E}_{\text{w_EMIC}}$ in the energy range of 14–30 keV and the pitch angle range of 33.75° – 78.75° was seen by all four spacecraft (Figure 3e). This demonstrates that the cyclotron resonance transferred energy from hot anisotropic (and nongyrotropic) protons. A large magnitude of negative $\mathbf{j} \cdot \mathbf{E}_{\text{w_EMIC}}$ appeared in the top two energy bins (Figures 3f and 3g) (For comparison, $\mathbf{j} \cdot \mathbf{E}_{\text{w_EMIC}}$ in the next two energy bins are also shown in Figures 3h and 3i.) Because the wave looks coherent around the large negative $\mathbf{j} \cdot \mathbf{E}_{\text{w_EMIC}}$, a spread of the large magnitude of negative $\mathbf{j} \cdot \mathbf{E}_{\text{w_EMIC}}$ in the pitch angle is likely caused by nonlinear trapping of resonant protons and a spatial variation of the magnetic field intensity (and other plasma parameters) that affects the dispersion relation of the EMIC wave and the resonance condition. Because the frequency variation of the EMIC wave is unclear (Figure S3a), the gradient of the magnetic field intensity along the field line (increase in magnetic field intensity with wave propagation) would mainly contribute to the nonlinear trapping of resonant protons with a negative $\mathbf{j} \cdot \mathbf{E}_{\text{w_EMIC}}$ (Omura et al., 2010). The nonlinear trapping of resonant protons will be discussed in detail in another manuscript.

The positive $\mathbf{j} \cdot \mathbf{E}_{\text{w_EMIC}}$ for ions moving in the opposite direction could be the effect of the Landau resonance. The Landau resonance condition ($=V_{\text{ph_para}}$) is also shown in Figure S2a. Note that because only the components of \mathbf{j} and $\mathbf{E}_{\text{w_EMIC}}$ perpendicular to \mathbf{B}_{0_EMIC} are considered in the present study, on average the protons are accelerated in the direction perpendicular to \mathbf{B}_{0_EMIC} due to the energy transfer. The interaction would be the same type as of the interaction between the oblique whistler-mode waves and electrons (Hsieh & Omura, 2017, 2018; Omura et al., 2019; Shklyar & Matsumoto, 2009). The small but non-zero amplitude of the z component of $\mathbf{B}_{\text{w_EMIC}}$ compared with the magnitude of the x - y component of \mathbf{B}_{0_EMIC} (Figure 3b) indicates that the wave normal angle of EMIC wave is slightly oblique ($\sim 22^\circ$ estimated in Appendix B).

The magnetic trough in the vicinity of Event 2 was a relatively large structure (long period of $B_{\text{w_ULF}_z}$) in the troughs (Figure 2a). An enhancement of EMIC waves was widely distributed in the large trough of magnetic field intensity (Figures 4a–4c). The EMIC wave tended to propagate southward (anti-parallel to the magnetic field) (Figure 4d). Thus, the situation was similar to Event 1. Negative $\mathbf{j} \cdot \mathbf{E}_{\text{w_EMIC}}$ in the energy range of 14–30 keV and the pitch angle range of 33.75° – 78.75° was seen around 12:18:30 UT by all four spacecraft (Figure 4e). For the background magnetic field intensity of 22.5 nT and $f_{\text{EMIC}} = 0.0851$ Hz ($=2/23.50$) as observed, $V_{\text{ph_para}}$ and V_{res} were calculated as ~ -320 and ~ 960 km/s, respectively (Appendix B). In the energy range of 18–30 keV, this V_{res} corresponds to the pitch angle of 59° – 66° (Figure S2b). A large magnitude of negative $\mathbf{j} \cdot \mathbf{E}_{\text{w_EMIC}}$ concentrated above ~ 18 keV (top two energy bins) (Figures 4f–4i). The detailed feature, especially nongyrotropic distribution of ions, in the vicinity of the minimum of $\mathbf{j} \cdot \mathbf{E}_{\text{w_EMIC}}$ was studied by Kitamura et al. (2018). In addition to the gradient of the magnetic field intensity along the field line, slight increase in time of the wave frequency ($\sim 12:18:10$ – $12:18:35$ UT in Figure S4a) would contribute to the nonlinear trapping of resonant protons with a negative $\mathbf{j} \cdot \mathbf{E}_{\text{w_EMIC}}$ (Omura et al., 2010).

4. Discussion

4.1. Size of EMIC Waves

Interestingly, the temporal variation of the Poynting flux observed by MMS4 in Event 1 preceded that observed by MMS1–3 by ~ 1 – 5 s (Figure 3d). If the EMIC wave is fixed in the mirror mode like structure, which is observed as the compressional ULF wave, moving westward with a velocity of ~ 40 km/s (Appendix A), the time difference must be ~ 3.5 s, because the position of MMS1–3 is ~ 140 km westward from MMS4. Thus, the EMIC wave was probably generated quasi-continuously (at least longer than the time scale of the passage of the spacecraft) at the magnetic trough and the variation of the magnitude of the Poynting flux was probably caused by a spatial effect (limited spatial extent of the EMIC wave). Such a measurement of an apparent wave packet (due not to temporal but to spatial effect) is similar to the situation for some whistler-mode waves in the compressional structures in the magnetosheath (Kitamura et al., 2020). Under the assumption that the observed variation of $\mathbf{j} \cdot \mathbf{E}_{\text{w_EMIC}}$ is also such a spatial effect, we can estimate the spatial extent along the direction of the propagation ($\sim -y$ in FAC) of the mirror mode like structure (compressional ULF wave) of the region where the energy transfer was occurring. The extent was ~ 920 ($\sim 1,740$) km on the basis of the velocity of ~ 40 km/s and the duration for which $\mathbf{j} \cdot \mathbf{E}_{\text{w_EMIC}}$ for the pitch angle of 33.75° – 78.75° and the energy range of 14–30 keV was more negative than 50% (10%) of the minimum value (Figure 3e). This extent is comparable with the diameter of cyclotron motion ($2 \times$ gyro-radius)

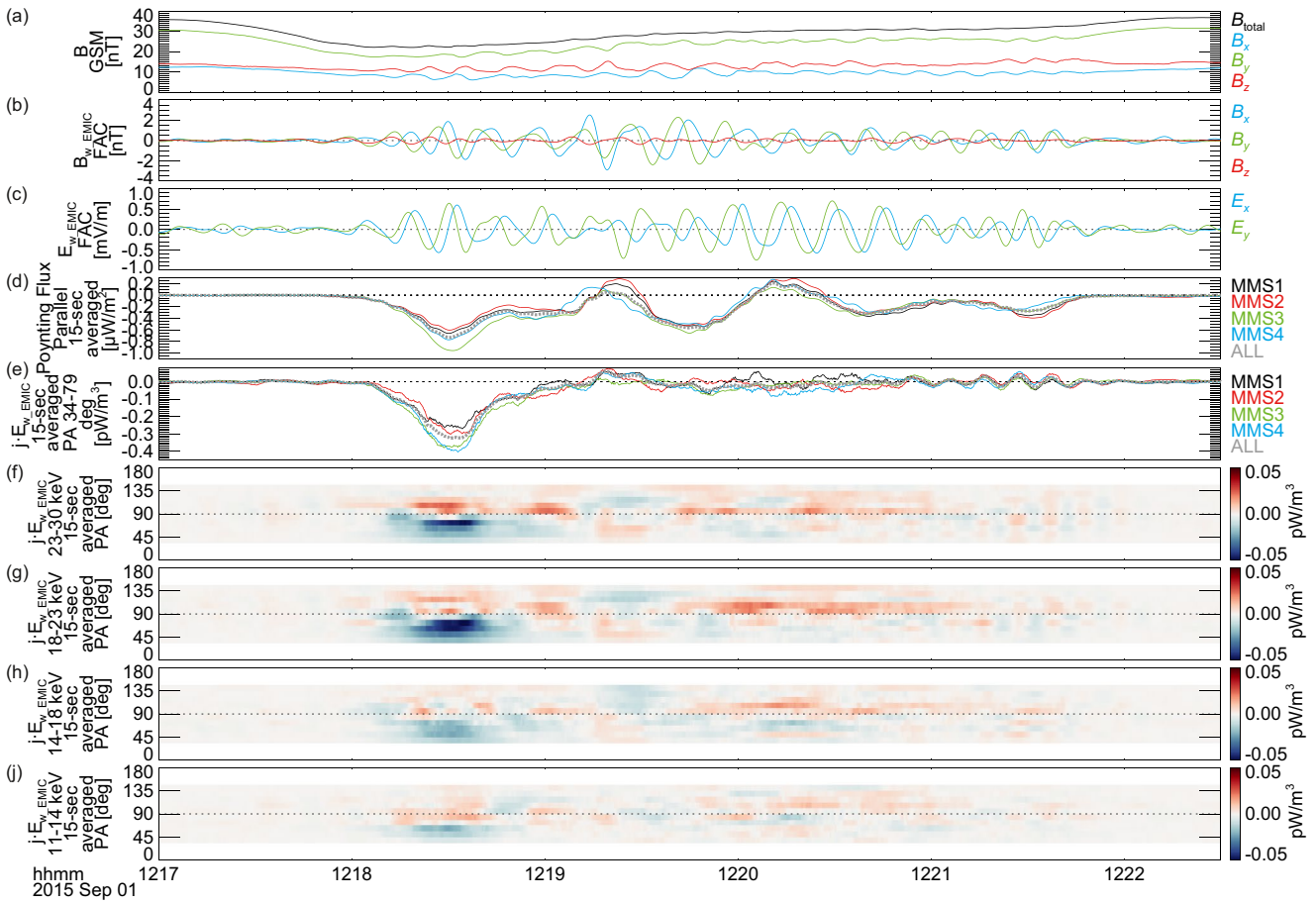


Figure 4. The detailed characteristics of the EMIC wave (Event 2). The format is the same as that of Figure 3. EMIC, electromagnetic ion cyclotron.

of protons that had a large magnitude negative $\mathbf{j} \cdot \mathbf{E}_{w_EMIC}$. For example, the gyro-radius of protons with an energy of 23 keV and a pitch angle of 50° is ~ 650 km in the vicinity of the minimum of magnetic field intensity (~ 26 nT). A large-amplitude EMIC wave (maximum $B_{w_EMIC}/B_{0_EMIC} \sim 0.08$) would be generated even in such a nonuniform region. J. Lee et al. (2013) reported that the typical coherent dimension of EMIC waves is 10–16 gyroradii of 100 keV protons. In the present case, the gyroradius of 100 keV protons with a pitch angle of 90° is 1,760 km, which is comparable with the spatial extent of the region where the energy transfer was occurring. Thus, the spatial extent can be much smaller than the typical scale of EMIC waves, and the modulation by the mirror mode like structure (compressional ULF wave) would produce such a small spatial extent.

Similar estimation of the spatial extent of the region where a large energy transfer occurred can be performed for Event 2, under the assumption that the observed variation of $\mathbf{j} \cdot \mathbf{E}_{w_EMIC}$ is a spatial effect. The extent was ~ 960 ($\sim 2,500$) km on the basis of the velocity of ~ 45 km/s and the duration for which $\mathbf{j} \cdot \mathbf{E}_{w_EMIC}$ for the pitch angle of 33.75° – 78.75° and the energy range of 14–30 keV was more negative than 50% (10%) of the minimum value (Figure 4e). In this case ($|B_{0_EMIC}| \sim 22.5$ nT), the gyro-radius of protons with an energy of 23 keV and a pitch angle of 63° (on the cyclotron resonance condition) is ~ 870 km. This extent is comparable with the diameter of cyclotron motion ($2 \times$ gyro-radius) of protons that had a large magnitude negative $\mathbf{j} \cdot \mathbf{E}_{w_EMIC}$. It is similar to the case of Event 1.

Interestingly, the region with a large magnitude of negative $\mathbf{j} \cdot \mathbf{E}_{w_EMIC}$ was localized as compared with the duration of the EMIC wave in Event 2 (Figure 4c and 4e). The region was close to the minimum of B_{0_EMIC} in the mirror mode like structure (compressional ULF wave), and the situation is similar to Event 1. Because of the much smaller magnitude of the z component of \mathbf{B}_{w_EMIC} than that of the x-y component of \mathbf{B}_{w_EMIC}

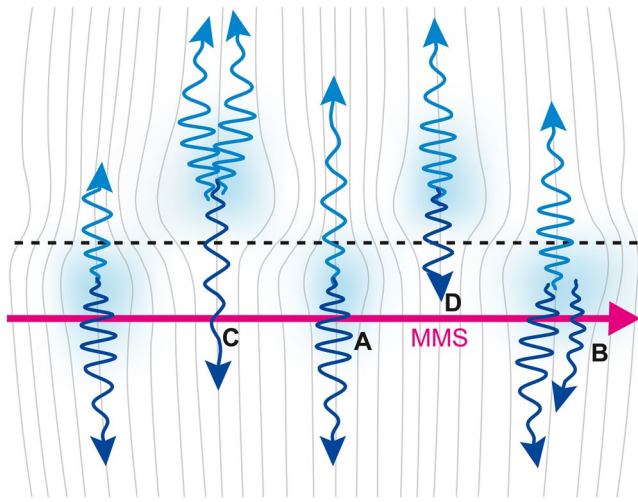


Figure 5. The schematic of the observed and expected features of ULF waves and EMIC waves. The dotted line is the location of the magnetic equator if the compressional structures do not exist. The compressional ULF waves probably have an antisymmetric standing structure about the magnetic equator as suggested by other studies (Baumjohann et al., 1987; L. Chen & Hasegawa, 1991; Cheng & Lin, 1987; Cheng & Qian, 1994; Korotova et al., 2013, 2009; Takahashi, Fennell et al., 1987; Takahashi, Lopez et al., 1987; Tian et al., 2020; Vaivads et al., 2001; X. Zhu & Kivelson, 1994). EMIC waves are expected to be generated in the vicinity of the minimum- B along field lines in the trough of magnetic field intensity and to propagate northward and southward. EMIC, electromagnetic ion cyclotron; ULF, ultralow frequency.

(Figure 4b), and the southward propagation, the propagation angle must be almost anti-parallel to \mathbf{B}_{0_EMIC} . Thus, the EMIC wave observed outside the region with a large magnitude negative $\mathbf{j} \cdot \mathbf{E}_{w_EMIC}$ was probably generated elsewhere, and would not be directly connected to the EMIC wave observed in the region with the large magnitude of negative $\mathbf{j} \cdot \mathbf{E}_{w_EMIC}$. Probably, there were multiple coherent EMIC waves with a spatial extent perpendicular to \mathbf{B}_{0_EMIC} much smaller than that of the single large trough of B_{0_EMIC} . Some differences in the Poynting flux among the spacecraft (Figure 4d), which had separations of only ~ 160 km, support this idea.

Note that it is not clear how often such a spatial effect becomes important for observations of wave packets. Probably, real temporal changes of the wave amplitude also produce wave packets. In some case, co-existence of multiple waves with different frequencies, as reported by X.-J. Zhang, Mourenas et al. (2020) for whistler mode waves, can also produce wave packets. On the basis of the present study, we suggest that very localized waves can also become a candidate of the causes of observed wave packets. Fully revealing the cause of each wave packet is difficult, and is beyond the scope of this study.

If the EMIC waves are spatially localized perpendicular to \mathbf{B}_{0_EMIC} , it will be difficult to detect an EMIC wave from a specific coherent source for a long time because of the small spatial extent of the EMIC wave and the drift of the background plasma (=motion of the compressional structure). For example, if an EMIC wave with a period of 15 s has no temporal amplitude variations with a transverse spatial extent of 1,500 km and the drift velocity of ~ 40 km/s is assumed, a spacecraft crossing the EMIC wave will observe a wave packet for a duration of 37.5 s, which corresponds to only 2.5 times the wave period. The apparent wave packet

observed by the spacecraft would then have a broad power spectrum in frequency, even if the EMIC wave in the plasma rest frame is perfectly coherent and has no temporal variation of the frequency and amplitude (infinitely narrow in the power spectrum). In Event 2, there were likely multiple coherent EMIC waves with a small spatial extent perpendicular to \mathbf{B}_{0_EMIC} in the single large trough of B_{0_EMIC} . Especially in such a case, we need to be careful when discussing detailed characteristics of the wave using observed wave spectra, and the observed waveform may appear not to be very coherent.

4.2. Entire Picture of the Mirror Mode like Structure (Compressional ULF Wave) and EMIC Waves

Other spacecraft observations of similar compressional structures (Korotova et al., 2013; Takahashi, Fennell et al., 1987; Takahashi, Lopez et al., 1987; Vaivads et al., 2001; X. Zhu & Kivelson, 1994) and theoretical studies (L. Chen & Hasegawa, 1991; Cheng & Lin, 1987; Cheng & Qian, 1994) indicate that the compressional structures have an antisymmetric standing structure about the magnetic equator (Figure 5). During the interval studied here, the parallel component of $\text{grad } B_{0_EMIC}$ was almost continuously negative (Figure S1g). Thus, the spacecraft stayed south of minimum- B along the field lines in the compressional structures, although we cannot prove the antisymmetric standing about the minimum- B directly from the observed data. Such an antisymmetric standing can explain the appearance of (weak) EMIC waves even in the vicinity of the peaks of observed B_{0_EMIC} , as discussed below.

The energy transfer from hot anisotropic protons to EMIC waves (negative $\mathbf{j} \cdot \mathbf{E}_{w_EMIC}$) by cyclotron resonance was detected only in the vicinity of the center of the troughs of B_{0_EMIC} (A and B in Figure 5). In some cases, there were multiple EMIC waves in a trough of B_{0_EMIC} as observed in Event 2 (B in Figure 5). A decrease in cyclotron resonance velocity due to a decrease in magnetic field intensity and an increase in hot proton pressure (and usually temperature anisotropy) in the upstream region in the vicinity of minimum- B along field lines can enhance the growth rate of EMIC wave in the linear stage and can enhance the local

nonlinear growth rate owing to an increase in number of particles around the cyclotron resonance velocity. The observed characteristics are consistent with the idea, although the usable burst data are limited (only two EMIC wave events).

Because the distribution functions of hot ions were almost symmetric about the pitch angle of 90° (Figures S1e and S2), the EMIC waves must be generated bi-directionally in the vicinity of the minimum- B along field lines in the regions of small magnetic field intensity in the compressional structures (Figure 5), although any asymmetry of gradient of the magnetic field intensity along the field line with respect to the minimum- B may cause asymmetry of nonlinear wave growth. If the antisymmetric standing of the compressional structure occurred as expected, the magnetic field lines in the vicinity of the peak of B_{0_EMIC} must be connected to a compressional structure on the northern side. If bi-directional EMIC waves are generated there and damping along the propagation path is not sufficiently strong, the EMIC waves may reach the location of the spacecraft on the southern side (C in Figure 5). If damping along the propagation path is large, EMIC waves would not be detected (D in Figure 5). The EMIC waves that appeared outside the trough of B_{0_EMIC} (relatively weak in most of the cases) may be explained by such propagation. Future investigations of not only the modulation of EMIC but also the energy transfer ($\mathbf{j} \cdot \mathbf{E}_{w_EMIC}$) will be necessary for a more robust understanding of the effect of mirror mode like structures (compressional ULF waves) on the EMIC waves.

The situation seems to be similar to that of whistler-mode waves that are frequently modulated by compressional structures in the magnetosheath (e.g., Ahmadi et al., 2018; Breuillard et al., 2018; Kitamura et al., 2020; Maksimovic et al., 2001; Smith et al., 1969; Smith & Tsurutani, 1976; Y. Zhang et al., 1998) and sometimes even in the magnetosphere (Baumjohann et al., 2000; Dubinin et al., 2007; W. Li et al., 2011; Tenerani et al., 2013; Xia et al., 2016; X.-J. Zhang, Angelopoulos et al., 2020; X.-J. Zhang, Chen et al., 2019). The EMIC waves were, however, detected even out of troughs of B_{0_EMIC} in the present study, whereas whistler-mode waves appear only in the trough of the magnetic field intensity in most of the cases. Perhaps, this difference is related to the propagation and/or damping outside of the troughs rather than the generation process. Such a perspective will be important for further progress in understanding of the effect of mirror mode like structures (compressional ULF waves) on higher frequency waves.

4.3. Condition of the Mirror Instability in ULF Waves

The condition of the mirror instability was satisfied only at the center of some troughs of magnetic field intensity (Figure 2d). Similar situations have been reported in many events in the magnetosphere (Korotova et al., 2009; Vaivads et al., 2001; X. Zhu & Kivelson, 1994) and sometimes even in the magnetosheath (Balikhin et al., 2009). Although some studies about compressional ULF waves with the antiphase relation stated that the ULF waves were not consistent with the mirror mode because the condition of the mirror instability was not satisfied (Nishi et al., 2018; Takahashi, Fennell et al., 1987), once a mirror mode structure is generated by the instability, the structure would not collapse soon even if the surrounding environment changes to the condition under which the mirror instability cannot grow. Statistical studies of mirror mode structure in the magnetosheath showed that there are significant numbers of mirror mode like structures that do not satisfy this condition (Génot et al., 2009; Soucek et al., 2008). This fact supports the possibility that the mirror structure would not collapse soon in the stable region. Thus, the observed feature of the ULF wave is consistent with the idea that the ULF wave was the structure generated by the mirror instability at a different time and location and drifted to the location of the spacecraft without collapsing.

We cannot rule out the possibility that the structure was generated locally by the effects that were not considered by Hasegawa (1969) (for example, coupling with ballooning mode (L. Chen & Hasegawa, 1991; Cheng & Qian, 1994)). It is also possible that the structure was mainly generated at a different location (near minimum- B ?), because the condition of the mirror instability might be more frequently satisfied at minimum- B along field lines where the magnetic pressure was lower and the ion pressure was higher than that at the spacecraft location. If rapid growth of mirror structures occurred simultaneously with the growth of EMIC waves, we could not conclude that the EMIC wave growth is modulated by mirror mode like structures (ULF wave), nonetheless, there is no evidence of rapid local growth of mirror mode like structures.

The compressional ULF waves were quasi-continuously detected for at least ~ 3 h. This would be the result of a passage of fairly stable structures rather than continuous observations of local rapid growth. Because MMS took 2–5 min to pass through a trough of magnetic field intensity, the time needed for the generation must have been longer than 2–5 min, if local generation was important. Thus, we believe that the EMIC wave growth (at least within ~ 5 min just before the observation) was probably modulated by (preexisting) mirror mode structures (ULF wave). Further detailed analysis of the generation process of the compressional ULF wave is beyond the scope of the present study.

4.4. Limitation for Understanding of the Wave Growth (or Damping) of EMIC Waves

The WPIA method used in the present study is a very powerful way to understand the detailed characteristics of wave-particle interactions. Recently some studies on waves (and/or turbulence) use current densities from the curlometer for calculation of $\mathbf{j} \cdot \mathbf{E}$ (Gershman, F-Viñas et al., 2017; He et al., 2019, 2020; Hull et al., 2020). Their method has an advantage in terms of being able to derive the total energy transfer rate. On the other hand, the method that focuses on partial $\mathbf{j} \cdot \mathbf{E}$ at the various parts of the distribution function, as used in the present and some other studies (C. H. K. Chen et al., 2019; T. C. Li et al., 2019; Katoh et al., 2013; Kitamura et al., 2018; Shoji et al., 2017), can resolve which part of the distribution function contributes to energy exchange with waves. The information is important to understand which types of interaction occur. During Event 1, positive $\mathbf{j} \cdot \mathbf{E}_{w_EMIC}$ around the Landau resonance velocity and negative $\mathbf{j} \cdot \mathbf{E}_{w_EMIC}$ around cyclotron resonance velocity appeared simultaneously. During Event 2, positive $\mathbf{j} \cdot \mathbf{E}_{w_EMIC}$ related to He^+ was reported by Kitamura et al. (2018) during the detection of negative $\mathbf{j} \cdot \mathbf{E}_{w_EMIC}$ around the cyclotron resonance velocity for protons. In such cases, the current from different interactions can cancel each other out, if one sees only the total current. Comparison between the total $\mathbf{j} \cdot \mathbf{E}$ that is obtained by the curlometer and partial $\mathbf{j} \cdot \mathbf{E}_{w_EMIC}$ that is obtained by the particle measurements will be an interesting subject for future studies.

It is possible to show the acceleration/deceleration of the particles in a distribution function because the partial $\mathbf{j} \cdot \mathbf{E}_w$ divided by partial number density corresponds directly to the rate of energy variation of particles at a certain part of the distribution function (Kitamura et al., 2018). In contrast, it is still difficult to investigate the growth/damping of the wave. The energy transferred to the wave is total $(-\mathbf{j} \cdot \mathbf{E}_w)$. This energy is partitioned into the local (in the plasma rest frame) increase in energy of the wave and convective growth of the wave. In cases where the single plane wave approximation with constant amplitude (perpendicular to wave number vector) is valid in a wide region or the drift velocity is small, if temporal variations of the amplitude exist, we can estimate the local increase in energy of the wave. In the present case, the EMIC waves were so localized in the troughs of magnetic field intensity that it was difficult to discriminate the local variation in the plasma rest frame from the spatial variation owing to the drift of plasma.

Because larger magnitude partial $\mathbf{j} \cdot \mathbf{E}_{w_EMIC}$ was detected around the upper energy limit (~ 30 keV) of FPI-DIS (Figures 3f and 4f), the energy transfer at the energy above 30 keV where the high temporal resolution measurements of ions with a full-sky field of view and a good angular resolution were not available (Blake et al., 2016; Mauk et al., 2016), could not be negligible for the total energy transfer. For a further complete understanding of total $\mathbf{j} \cdot \mathbf{E}_{w_EMIC}$ in the future, measurements in the energy range of ~ 10 – 100 keV with a good angular resolution will be important. Now, the energy range is covered by, for example, the energetic ion spectrometer (Mauk et al., 2016) on MMS and the medium-energy particle experiments–ion mass analyzer (Yokota et al., 2017) on the Arase satellite. To cover multiple gyro-phases in this energy range, mass installation of such instruments on one spacecraft, such as FPI on MMS, will be ideal, which should be considered in future missions.

In the present study, we have analyzed the component of $\mathbf{j} \cdot \mathbf{E}_{w_EMIC}$ perpendicular to \mathbf{B}_{0_EMIC} . Direct measurements of electric fields in the low-frequency range are still technically challenging, especially for the component parallel to the magnetic field. The Landau resonance with the component of \mathbf{E}_{w_EMIC} parallel to \mathbf{B}_{0_EMIC} that could not be measured might also cause some energy exchange between protons and the EMIC wave. This will become important, especially in cases where the wave normal angle becomes large. Note that the wave normal angles were not very large ($< 22^\circ$) in Events 1 and 2.

Background thermal electrons can also interact with EMIC waves by the Landau resonance (B. Wang et al., 2019; Yuan et al., 2014; Zhou et al., 2013). Low-energy electrons ($\sim 10\text{--}50$ eV in Figure S1a) had field-aligned distribution (not shown) and might be generated by such an interaction. Nevertheless, there were no clear one-to-one correspondences with the EMIC waves (Figure S1a). Thus, strong interaction might occur at different locations (at higher latitudes?) or different times, or it might be the integrated result of many weak interactions with many EMIC waves on the time scale much longer than each wave packet. These Landau type interactions will also be the subject of future studies.

There are still other types of wave-particle interactions. Although the EMIC waves can strongly interact with relativistic electrons (e.g., Albert & Bortnik, 2009; Kubota & Omura, 2017; Miyoshi et al., 2008; Nakamura et al., 2019; H. Zhu et al., 2020), especially in the outer magnetosphere, relativistic electron fluxes are extremely small and the relativistic electrons definitely do not contribute to the total $\mathbf{j} \cdot \mathbf{E}_{w,EMIC}$. There might be some non-resonant energy transfers between cold (plume) protons and the EMIC wave. A full understanding of all the various types of interaction will be needed to quantify the total energy transfer rate. The present study is the first step of such an attempt.

5. Conclusions

The MMS spacecraft observed compressional ULF waves and EMIC waves simultaneously in the late afternoon (MLT: 15.9–16.2 h) outer magnetosphere (dipole- L : 11.7–12.9). Because of the high background plasma density of $\sim 5/\text{cm}^3$ in the vicinity of the enhancements of the EMIC waves, the region was probably in the vicinity of the eastward edge of a plasmaspheric plume where the EMIC waves have been believed to be active (e.g., L. Chen et al., 2010; Fok et al., 2016; Jordanova et al., 2007; Kozyra et al., 1997) (Appendix C). The high background plasma density probably played an important role in the appearance of EMIC waves. Although the magnitude of MLAT was not small (-23.3° – -23.6°), the location of MMS was close ($\sim 1.5 R_E$) to the minimum- B along field lines (Kitamura et al., 2018). The geomagnetic condition was not active, and there were no sudden changes in solar wind dynamic pressure.

For the ULF wave, which had the period of about 2–5 min and the plasma β of order of 1, the magnetic pressure and the plasma (mostly ion) pressure were in antiphase, such that the total pressure remained almost constant. The ion temperature ratio ($T_{i,perp}/T_{i,para}$) tended to have peaks in the troughs of magnetic field intensity. Because the fluctuations of the magnetic field gradient were mostly in the azimuthal direction (y -component in FAC), the troughs of magnetic field intensity in the compressional ULF wave probably had been elongated along the magnetic field and radial directions (Appendix A). The analysis by the multi-spacecraft timing method (TM) indicates that the ULF wave (mirror mode like structure) tended to move westward almost continuously with a velocity of $\sim 30\text{--}50$ km/s (Appendix A). This velocity is close to the background plasma velocity, and the westward propagation velocity in the plasma rest frame was very slow (< 20 km/s). The wavelength of the structure is estimated as $\sim 3,600\text{--}9,000$ km that corresponds to the azimuthal wave number m of ~ -55 – -140 . Because the propagation direction was sunward, the source of the ULF wave was unlikely at the dayside magnetopause. This is different from the case reported by S. Liu et al. (2019). Based on the observations, anisotropic ions coming from the nightside, which were probably injected from the plasma sheet due to gradual convection and/or small substorms (the AL index > -154 nT), seem to be the energy source for the ULF (and EMIC) wave generation. These characteristics are consistent with the idea that the compressional ULF fluctuations are generated by the mirror mode type instability. Nevertheless, the condition of the mirror instability was satisfied only at the center of some troughs of magnetic field intensity. This is similar to the situations of some other observations of mirror mode like structures (Korotova et al., 2009; Vaivads et al., 2001). If the wave structure was generated by the mirror instability, the structure has probably been generated at the different time and/or location, although the possibility of local generation due to effects not considered by Hasegawa (1969) cannot be completely denied.

Many enhancements of He-band EMIC waves (below the cyclotron frequency of He^+) were detected in the vicinity of the troughs of the magnetic field intensity, although (weak) EMIC waves appeared even in the vicinity of the peaks of the magnetic field intensity. An antisymmetric standing compressional structure (observed as ULF waves) (Baumjohann et al., 1987; Korotova et al., 2009, 2013; Takahashi, Fennell et al., 1987; Takahashi, Lopez et al., 1987; Tian et al., 2020; Vaivads et al., 2001; X. Zhu & Kivelson, 1994)

and EMIC wave generation (and propagation) at the side opposite to that of the observation (Figure 5) can explain the feature. At least, during the two events when the burst data are available, the energy transfer from hot protons to the EMIC wave (negative $\mathbf{j} \cdot \mathbf{E}_{w_EMIC}$) around the cyclotron resonance condition was identified only in the vicinity of the center of the troughs of magnetic field intensity. It is consistent with the idea that the energy transfer responsible for the generation of the EMIC waves is modulated by the mirror mode like structure (compressional ULF wave). For deriving the total energy transfer rate, which is the most important factor for wave growth, it will be necessary to understand all various types of interactions. The present study that investigated important parts of partial energy transfer rate in the ion distribution function is the first phase of such an attempt. The observed feature of the energy transfer around the cyclotron resonance suggests that the growth of the EMIC wave was modulated by the mirror mode like structure (compressional ULF wave).

A decrease in the cyclotron resonance velocity due to a decrease in magnetic field intensity and an increase in hot proton pressure in the troughs of magnetic field intensity can enhance the growth rate of EMIC waves in the initial stage of linear growth in the upstream region (Loto'aniu et al., 2009). Additionally, in many cases, an increase in temperature anisotropy of ions that were dominated by protons in the troughs of magnetic field intensity would raise the linear growth rate of EMIC waves. Furthermore, the decrease in cyclotron resonance velocity and the increase in hot proton pressure will lead to an increase in number of particles around the cyclotron resonance velocity, raising the nonlinear growth rate. Because the identified $\mathbf{j} \cdot \mathbf{E}_{w_EMIC}$ is due to the nongyrotropy of protons (Kitamura et al., 2018), the energy transfer identified in the present study is of the nonlinear part of the growth of EMIC waves (e.g., Omura et al., 2010).

The regions where protons around the cyclotron resonance condition had clear negative $\mathbf{j} \cdot \mathbf{E}_{w_EMIC}$ would be very narrow (only a few times the gyroradii of hot resonant protons) at least in azimuthal (MLT) direction in the mirror mode like structure (compressional ULF wave), if the temporal variation came from the spatial effect (drift motion of the background plasma perpendicular to the background magnetic field). This may produce apparent wave packets observed by a spacecraft and cause a broadening in frequency in the power spectrum. Considering the possibility of localization of EMIC waves will be important to understand the observed wave packets. How often such localization produces apparent wave packets is left for future studies.

Clear positive $\mathbf{j} \cdot \mathbf{E}_{w_EMIC}$ was identified around the Landau resonance velocity in Event 1 with a slightly oblique wave normal angle ($\sim 22^\circ$) (At least around this time interval, measurements by all four individual spacecraft showed clear positive $\mathbf{j} \cdot \mathbf{E}_{w_EMIC}$ simultaneously (not shown).) This is likely a sign of the beginning of the damping, and the location of the observation may have been near the end of the convective growth of the EMIC wave. Around the time interval when the magnitude of $\mathbf{j} \cdot \mathbf{E}_{w_EMIC}$ was large, the wave propagating away from the minimum- B along the field line was dominant. The situation was likely very fortunate for the use of the WPIA method. In the vicinity of the center of wave source, the forward- and backward-propagating waves may frequently exist simultaneously with comparable amplitudes. In such cases, it can be difficult to discriminate \mathbf{E}_{w_EMIC} for one of the waves from that of another wave, although such discrimination is necessary to evaluate $\mathbf{j} \cdot \mathbf{E}_{w_EMIC}$ for the wave growth or damping. Thus, similar investigations will be possible only in the region where one of the EMIC waves is dominant and at times before the end of nonlinear convective wave growth.

Appendix A: Shape and Propagation of Compressional ULF Waves

Because the fluctuations of the magnetic field gradient ($\text{grad } B_{0_EMIC}$) were dominated by the y component in FAC (Figure S1g) the troughs of magnetic field intensity in the compressional ULF wave probably had been elongated along the magnetic field and radial directions (knife-blade or pancake shape (Figure 1 of Fadanelli et al., (2019))). This characteristic of the compressional ULF wave is similar to some other spacecraft observations in the magnetosphere (Korotova et al., 2009, 2013; Tian et al., 2020). Note that the gradient larger than ~ 0.6 pT/km is reliable, because the accuracy of FGM is ~ 0.1 nT (Russell et al., 2016) and the separation of the MMS spacecraft was ~ 160 km around Event 1 and Event 2 (Figure 1). As can be seen in Figures A1a and A1b, the changes in z component of \mathbf{B}_{w_ULF} ($B_{w_ULF_z}$) observed by MMS4, which was

located eastward (+y) from the others (Figure 1), preceded that observed by MMS1–3. This fact means that the compressional ULF wave propagated westward.

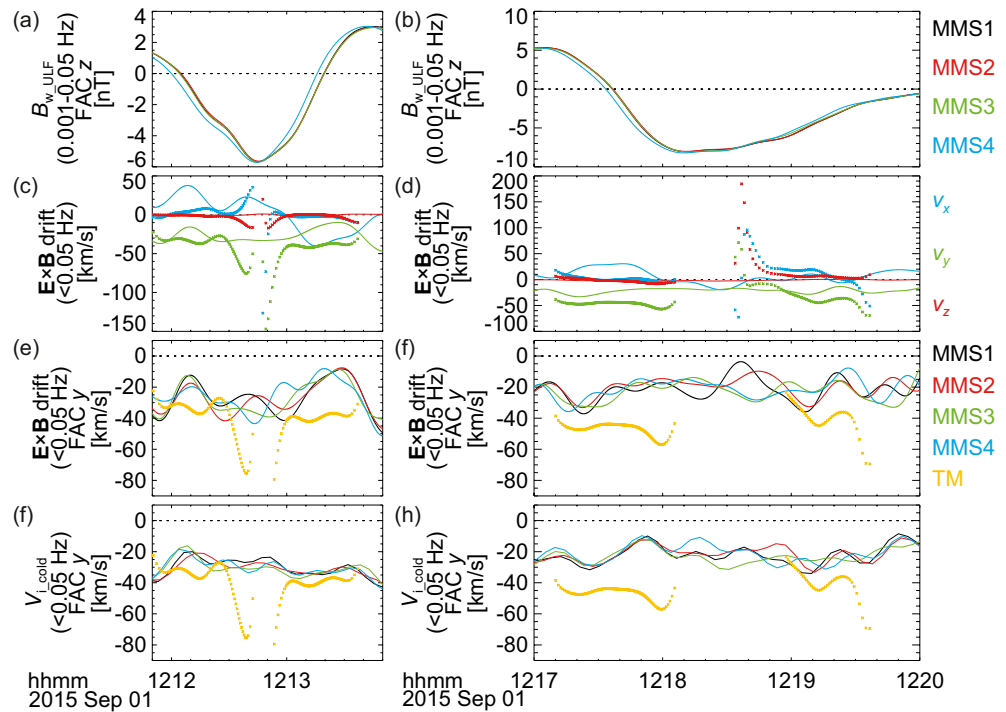


Figure A1. The waveform of the magnetic fields in the frequency range of 0.001–0.05 Hz ($\mathbf{B}_{w,ULF}$) and velocities related to background plasma motion and the ULF wave around the EMIC wave events. (a and b) Compressional (z in FAC) component of waveforms of $\mathbf{B}_{w,ULF}$, (c and d) $\mathbf{E} \times \mathbf{B}$ drift velocity (curves) and wave normal velocities (crosses) calculated by timing method (TM) of the waveform of $B_{w,ULF,z}$ in FAC, (e and f) azimuthal (y in FAC) component of $\mathbf{E} \times \mathbf{B}$ drift velocities and wave normal velocities, and (g and h) azimuthal (y in FAC) component of cold ion velocity and wave normal velocities. EMIC, electromagnetic ion cyclotron; FAC, field-aligned coordinates; ULF, ultralow frequency.

The hot (14–30 keV) component of ions had the highest differential energy fluxes (Figure A2a). The hot ions around the direction perpendicular to $\mathbf{B}_{0,EMIC}$ (pitch angle: 78.75°–101.25°), which had the highest differential energy fluxes (Figure A2b), became nongyrotropic (Figure A2c) in the vicinity of a large temporal change of $B_{w,ULF,z}$ that must be caused by a large magnitude y (azimuthal) component of $\text{grad } B_{0,EMIC}$ (Figures A2d and A2e). An ion sounding technique can be applied to this nongyrotropy to estimate the shape and propagation of compressional ULF waves (Korotova et al. 2009, 2013; N. Lin et al., 1988; Su et al., 1977; Takahashi, Lopez et al., 1987; Vaivads et al., 2001; X. Zhu & Kivelson, 1994). Variations of ions coming from the $-x$ direction (180° in Figure A2c), which correspond to the ions with their gyrocenters eastward of the spacecraft, preceded those coming from the other directions. In many cases, differential energy fluxes of ions coming from +y and $-y$ directions (90° and 270° in Figure A2c) showed similar variations. These characteristics are consistent with the expectation from the fluctuations of $\text{grad } B_{0,EMIC}$ that the troughs of magnetic field intensity in the compressional ULF wave probably had been elongated along the radial direction, as discussed in the last paragraph.

If the compressional ULF wave can be regarded as a plane wave locally, the multi-spacecraft timing method can be used to derive the normal direction and velocity along the normal vector. First, increments of 0.1 nT in the compressional component $B_{w,ULF,z}$ were used as thresholds. As the reference times, we identified the times when $B_{w,ULF,z}$ crossed one of the increments. If $|dB_{w,ULF,z}/dt| > 0.05$ nT/s at the crossing, times for TM were searched for $B_{w,ULF,z,MMS1-4}$ within 15 s of each reference time. If the times for the same increment crossing were found for all four spacecraft, the velocity along the normal vector was calculated as the solution to the system of three equations about the separation vectors at the reference time and the timing

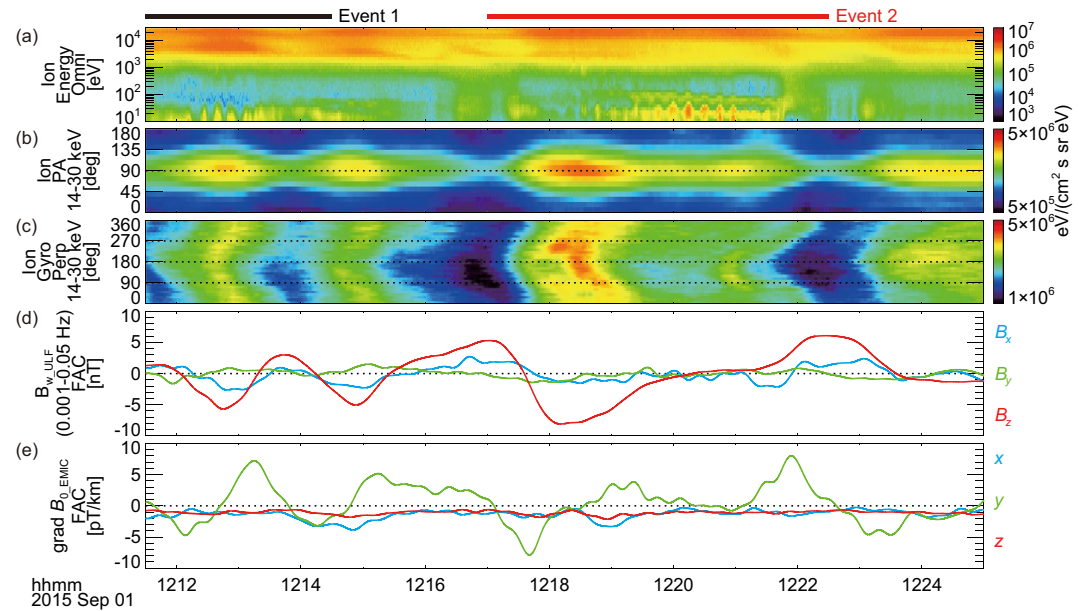


Figure A2. Features of ions and gradient of the magnetic field intensity around Event 1 and Event 2. (a) Omnidirectional energy-time spectrum of ions, (b) 15-s moving averaged pitch angle-time spectrum of hot ions (14–30 keV), (c) 15-s moving averaged gyro angle-time spectrum of hot ions around the pitch angle of 90°, (d) wave components of the magnetic field in the frequency range of 0.001–0.05 Hz (\mathbf{B}_{w_ULF}), and (e) gradient of the magnetic field intensity ($\text{grad } B_{0_EMIC}$). In the gyro angle-time spectrogram, ions observed at 0° and 90° correspond to ions that go toward x and y directions in FAC, respectively. The intervals shown in Figure 3 (Event 1) and 4 (Event 2) are indicated by black and red bars, respectively, above the panels. FAC, field-aligned coordinates.

differences (MMS2–1, 3–1, and 4–1) (Schwartz, 1998). To get the timing difference as accurate as possible, the data points of $B_{w_ULF_z}$ and $B_{w_ULF_z_MMS1-4}$ were linearly interpolated.

Figures A1c and A1d indicate that the propagation directions derived by TM tend to be very close to $-y$ (westward) except for short fluctuations around the trough of $B_{w_ULF_z}$, which is discussed in the next paragraph, and the velocity was $\sim 30\text{--}50$ km/s in the vicinity of the middle of large variations of $B_{w_ULF_z}$. The westward velocities are almost equal to or slightly larger than the low pass filtered (<0.05 Hz) $\mathbf{E} \times \mathbf{B}$ drift velocity. Note that the accuracy of the electric field measurements is ~ 0.5 mV/m (Lindqvist et al., 2016), which corresponds to the $\mathbf{E} \times \mathbf{B}$ drift velocity of 20 km/s for the magnetic field intensity of 25 nT. Thus, some of the differences between the normal velocity from TM and the $\mathbf{E} \times \mathbf{B}$ drift velocity might come from the limitation in the accuracy of electric field measurements, and thus detailed comparison may be difficult. Because the magnitude of the y component of the normal velocity sometimes exceeded the range of the difference among the spacecraft in the low pass filtered $\mathbf{E} \times \mathbf{B}$ drift velocity (Figures A1e and A1f) and/or bulk velocity of cold ions (10–257 eV) (Figures A1g and A1h) among the spacecraft in the negative direction, the compressional ULF wave probably propagated westward very slowly (<20 km/s) even in the plasma rest frame. This almost zero or small westward velocity in the plasma rest frame is consistent with the results from other observational studies on compressional ULF waves (Baumjohann et al., 1987; Constantinescu et al., 2009; Korotova et al., 2009, 2013; Takahashi, Fennell et al., 1987; Takahashi, Lopez et al., 1987; Tian et al., 2020). Thus, the compressional ULF wave itself is probably one of the typical events. The authors of these manuscripts stated that the most likely source of the waves is the mirror instability.

Although the wave normal directions and velocities calculated by the timing method show fluctuations around the center of the troughs of $B_{w_ULF_z}$ (Figures A1c–A1h), the duration of such fluctuations is much shorter than the period of the compressional ULF wave. Thus, such fluctuations may be caused by localized structures with a spatial scale much smaller than the compressional ULF wave. If the plane wave approximation becomes invalid in the spatial scale of the spacecraft separation (~ 160 km), the wave normal directions and velocities calculated by the timing method become unreliable.

Because the phase difference of $B_{w_ULF_z}$ among the spacecraft is small (Figure S5a), the wavelength of the ULF wave must be much larger than the spacecraft separation (~ 160 km). Figures S5b–S5d indicate that the y component of the normal velocity derived from TM, the low pass filtered $\mathbf{E} \times \mathbf{B}$ drift velocity, and the bulk velocity of cold ions tended to stay around -30 km/s, when the normal velocity derived from TM was almost stable and cold ions (a few tens of eV) were detected (sometimes around 11:10 and $\sim 11:50$ – $12:23$ UT in Figure S1b). Some short fluctuation of the wave normal velocities from TM without fluctuations of the drift velocity nor ion drift velocity can be explained by the same way as that discussed in the last paragraph. Because the period of the ULF wave was ~ 2 – 5 min, the wavelength is estimated as $\sim 3,600$ – $9,000$ km that corresponds to the azimuthal wave number m from ~ -55 to -140 .

Appendix B: Wave Number and Wave Normal Angle of EMIC Waves

Because there are four-point data, we can derive the wave number vector (\mathbf{k}) and the wavelength ($\lambda = 2\pi/k$, $k = |\mathbf{k}|$), if we can identify the phase differences between three pairs of spacecraft or the phase difference between one pair provided the information on the direction of \mathbf{k} (Pakhotin et al., 2013; Walker & Moiseenko, 2013). In the present cases, the phase is calculated in x - y (perpendicular to \mathbf{B}_{0_EMIC}) plane, and the phase difference from MMS1, which was located upstream (north) from the others, was computed. However, because the difference in \mathbf{B}_{w_EMIC} was small, it is difficult to derive a phase difference accurately, especially for the pairs of MMS3–1 and MMS4–1 (Figures S3b–S3d and S4b–S4d). Thus, we used minimum variance analysis to derive the wave normal angle and used the phase differences between MMS1 and MMS2 to derive k .

For Event 1, a minimum variance analysis was performed for \mathbf{B}_{w_EMIC} from 12:12:33.82 to 12:12:59.83 UT (26.01 s), which includes two rotation of \mathbf{B}_{w_EMIC} . We used a very short window because the minimum variance analysis can give misleading results, if the window includes multiple wave packets whose orientations are not constant (Anderson et al., 1996; Denton et al., 1996). The minimum variance direction corresponding to the direction of \mathbf{k} is $(x, y, z) = (0.3212, -0.1996, -0.9257)$ in FAC, which is $\sim 22^\circ$ from the direction anti-parallel to \mathbf{B}_{0_EMIC} (Figure 1a). The vector with $z < 0$ was chosen because of the negative (southward) Poynting flux (Figure 3d). This direction is close ($\sim 13^\circ$) to the separation between MMS1 and 2. Using the average of the phase difference (13.4°) and separation along \mathbf{k} (149 km), we obtain k of $\sim 1.6 \times 10^{-3}$ rad/km and λ of 4,000 km. The wavelengths parallel and perpendicular to \mathbf{B}_{0_EMIC} (λ_{para} , λ_{perp}) are $\sim 4,300$ km and $\sim 11,000$ km, respectively. For the background magnetic field intensity of 26 nT and the wave frequency ($f_{EMIC} = \omega_{EMIC}/2\pi$) of 0.0769 Hz ($= 2/26.01$), the parallel components of the phase velocity ($V_{ph_para} = \omega/k_{para} = f_{EMIC}\lambda_{para}$) and the cyclotron resonance velocity ($V_{res} = (\omega_{EMIC} - \Omega_{c_H+})/k_{para} = (f_{EMIC} - f_{c_H+})\lambda_{para}$) are calculated as ~ -330 and $\sim 1,370$ km/s, respectively.

For Event 2, a minimum variance analysis was performed for \mathbf{B}_{w_EMIC} from 12:18:15.20 to 12:18:38.70 UT (23.50 s), which includes two rotation of \mathbf{B}_{w_EMIC} . The estimated direction of \mathbf{k} is $(x, y, z) = (-0.1384, 0.0016, -0.9904)$ in FAC, which is only $\sim 8^\circ$ from the direction anti-parallel to \mathbf{B}_{0_EMIC} (Figure 1b). Using the average of the phase difference (12.8°) between MMS1 and 2 and the separation along \mathbf{k} (132 km), we obtain k_{para} of $\sim 1.7 \times 10^{-3}$ rad/km and λ_{para} of 3,700 km. For the background magnetic field intensity of 22.5 nT and $f_{EMIC} = 0.0851$ Hz ($= 2/23.50$), V_{ph_para} and V_{res} are calculated as ~ -320 and ~ 960 km/s, respectively.

Appendix C: EMIC Waves and Background Plasma Density

The event of the present study was observed probably in the vicinity of the eastward edge of a plasmaspheric plume. The spacecraft was located in the late afternoon MLT sector (~ 16 h MLT) where high-density plasma tends to appear most frequently and is likely related to the plasmaspheric plume (Chappell, 1974; S. H. Chen & Moore, 2006; Darrouzet et al., 2008; J. H. Lee & Angelopoulos, 2014). The eastward edge of the plasmaspheric plume is expected to be the best location for the growth of EMIC waves according to modeling studies (e.g., L. Chen et al., 2010; Fok et al., 2016; Jordanova et al., 2007; Kozyra et al., 1997). Note that the effect of the plasmaspheric plumes on the occurrence of EMIC waves is still a topic of observational investigations (Fraser & Nguyen, 2001; Halford et al., 2015; G.-J. Kim et al., 2016; Tetrack et al., 2017; Usanova et al., 2013).

To investigate the background plasma density, high-frequency electric field spectra with a temporal resolution of 16 s and spacecraft potential data (32 Hz sampling in the fast survey) from EDP on MMS1 are used. Although ASPOC was on for the interval of observation of EMIC waves and ULF waves, we can see the variation of the background plasma density on the basis of the variation of the spacecraft potential (Andriopoulou et al., 2016, 2018; Torkar et al., 2019). When the spacecraft potential was $\sim 3.2\text{--}3.4$ V (Figure S1h), an enhancement of electric field waves was seen around ~ 20 kHz (Figure S1i), which must be close to the electron plasma frequency. Thus, the background plasma density was $\sim 5/\text{cm}^3$ in the vicinity of the enhancements of the EMIC waves. This level of the background plasma density is comparable to that of typical plasmaspheric plumes (J. H. Lee & Angelopoulos, 2014; S. H. Lee et al., 2016; Walsh et al., 2013). Because a low-frequency cutoff of weak wave emissions (10–15 kHz), which probably corresponds to the L-O mode cutoff (=electron plasma frequency) or the R-X mode cutoff (\sim electron plasma frequency in the present case), can be seen around 10 kHz after $\sim 12:25$ UT (Figure S1i), the background plasma density probably reduced to the order of $1/\text{cm}^3$. This time corresponds to an increase in spacecraft potential, which is consistent with a decrease in background plasma density. This region would be in the vicinity of the eastward edge of a plasmaspheric plume (or plasmopause of very inflated plasmasphere). Although it is difficult to discriminate the edges of a plasmaspheric plume and plasmopause, the dipole L -value of ~ 13 at the density decrease is much larger than the typical location of the plasmopause ($L \sim 6$) under quiet geomagnetic conditions (Kwon et al., 2015). He-band EMIC waves disappeared after $\sim 12:22$ UT (Figure S1f). There were only a limited number of weak enhancements of H-band EMIC waves after 12:30 UT, although the compressional ULF waves are observed at least until 13:30 UT (not shown). Thus, the high background plasma density probably played an important role for the appearance of EMIC waves. On the other hand, because the spacecraft potential (background plasma density) does not show a clear correlation with the compressional ULF wave (Figure S1h), the plasma density is unlikely the main cause of the appearance and disappearance of EMIC waves in the compressional ULF wave (mirror mode like structure).

Acknowledgments

This research was supported by the National Aeronautics and Space Administration (NASA) Magnetospheric Multiscale Mission (MMS) in association with NASA contract NNG04EB99 C. The authors thank the entire MMS team and instrument leads for data access and support. The authors acknowledge C. J. Pollock, W. R. Paterson, J.-A. Sauvaud, V. N. Coffey, J. C. Dorelli, L. A. Avakov, B. Lavraud, M. O. Chandler, A. C. Barrie, and C. Schiff for their valuable roles in providing instrumentation and data production/quality of Fast Plasma Investigation. Institut de Recherche en Astrophysique et Planétologie (IRAP) contributions to MMS FPI was supported by Centre National d'Études Spatiales (CNES) and Centre National de la Recherche Scientifique (CNRS). The authors acknowledge R. B. Torbert for the use of electric field data and the selection of the burst data. This research was supported by Grants-in-Aid for Scientific Research (17H06140, 20H01959) of Japan Society for the Promotion of Science (JSPS). The authors gratefully acknowledge Eric Grimes and the development team of the Space Physics Environment Data Analysis System (SPEDAS) software (Angelopoulos et al., 2019) for their fruitful efforts in providing this software for our use. The authors thank J. King and N. Papitashvili of the National Space Science Data Center (NSSDC) in the NASA/GSFC for the use of the OMNI 2 data set (OMNI data from <http://omniweb.gsfc.nasa.gov/>).

Data Availability Statement

The data presented in this study are the Level-2 data of MMS, which can be accessed from MMS Science Data Center (<https://lasp.colorado.edu/mms/sdc/public/>).

References

- Ahmadi, N., Germaschewski, K., & Raeder, J. (2016). Effects of electron temperature anisotropy on proton mirror instability evolution. *Journal of Geophysical Research: Space Physics*, 121, 5350–5365. <https://doi.org/10.1002/2016ja022429>
- Ahmadi, N., Wilder, F. D., Ergun, R. E., Argall, M., Usanova, M. E., Breuillard, H., et al. (2018). Generation of electron whistler waves at the mirror mode magnetic holes: MMS observations and PIC simulation. *Journal of Geophysical Research: Space Physics*, 123, 6383–6393. <https://doi.org/10.1029/2018ja025452>
- Albert, J. M., & Bortnik, J. (2009). Nonlinear interaction of radiation belt electrons with electromagnetic ion cyclotron waves. *Geophysical Research Letters*, 36, L12110. <https://doi.org/10.1029/2009gl038904>
- Allen, R. C., Zhang, J.-C., Kistler, L. M., Spence, H. E., Lin, R.-L., Dunlop, M. W., & André, M. (2013). Multiple bidirectional EMIC waves observed by Cluster at middle magnetic latitudes in the dayside magnetosphere. *Journal of Geophysical Research: Space Physics*, 118, 6266–6278. <https://doi.org/10.1002/jgra.50600>
- Allen, R. C., Zhang, J.-C., Kistler, L. M., Spence, H. E., Lin, R.-L., Klecker, B., et al. (2015). A statistical study of EMIC waves observed by Cluster: 1. Wave properties. *Journal of Geophysical Research: Space Physics*, 120, 5574–5592. <https://doi.org/10.1002/2015ja021333>
- Allen, R. C., Zhang, J.-C., Kistler, L. M., Spence, H. E., Lin, R.-L., Klecker, B., et al. (2016). A statistical study of EMIC waves observed by Cluster: 2. Associated plasma conditions. *Journal of Geophysical Research: Space Physics*, 121, 6458–6479. <https://doi.org/10.1002/2016ja022541>
- Anderson, B. J., Denton, R. E., & Fuselier, S. A. (1996). On determining polarization characteristics of ion cyclotron wave magnetic field fluctuations. *Journal of Geophysical Research*, 101(A6), 13195–13213. <https://doi.org/10.1029/96JA00633>
- Anderson, B. J., & Fuselier, S. A. (1994). Response of thermal ions to electromagnetic ion cyclotron waves. *Journal of Geophysical Research*, 99(A10), 19413–19425. <https://doi.org/10.1029/94ja01235>
- Andriopoulou, M., Nakamura, R., Torkar, K., Baumjohann, W., Torbert, R. B., Lindqvist, P.-A., et al. (2016). Study of the spacecraft potential under active control and plasma density estimates during the MMS commissioning phase. *Geophysical Research Letters*, 43, 4858–4864. <https://doi.org/10.1002/2016GL068529>
- Andriopoulou, M., Nakamura, R., Wellenzohn, S., Torkar, K., Baumjohann, W., Torbert, R. B., et al. (2018). Plasma density estimates from spacecraft potential using MMS observations in the dayside magnetosphere. *Journal of Geophysical Research: Space Physics*, 123, 2620–2629. <https://doi.org/10.1002/2017JA025086>
- Angelopoulos, V., Cruce, P., Drozdov, A., Grimes, E. W., Hatzigeorgiou, N., King, D. A., et al. (2019). The Space Physics Environment Data Analysis System (SPEDAS). *Space Science Reviews*, 215, 9. <https://doi.org/10.1007/s11214-018-0576-4>
- Balikhin, M. A., Sagdeev, R. Z., Walker, S. N., Pokhotelov, O. A., Sibeck, D. G., Beloff, N., & Dudnikova, G. (2009). THEMIS observations of mirror structures: Magnetic holes and instability threshold. *Geophysical Research Letters*, 36, L03105. <https://doi.org/10.1029/2008GL036923>

- Barfield, J. N., & Coleman, P. J. (1970). Storm-related wave phenomena observed at the synchronous, equatorial orbit. *Journal of Geophysical Research*, 75(10), 1943–1946. <https://doi.org/10.1029/JA075i001p01943>
- Barfield, J. N., & McPherron, R. L. (1972). Investigation of interaction between Pc 1 and 2 and Pc 5 micropulsations at the synchronous orbit during magnetic storms. *Journal of Geophysical Research*, 77(25), 4707–4719. <https://doi.org/10.1029/JA077i025p04707>
- Barrie, A. C., Smith, D. L., Elkington, S. R., Sternovsky, Z., Silva, D., Giles, B. L., & Schiff, C. (2019). Wavelet compression performance of MMS/FPI plasma count data with plasma environment. *Earth and Space Science*, 6, 116–135. <https://doi.org/10.1029/2018EA000430>
- Barrie, A. C., Smith, S. E., Dorelli, J. C., Gershman, D. J., Yeh, P., Schiff, C., & Avakov, L. A. (2017). Performance of a space-based wavelet compressor for plasma count data on the MMS fast plasma investigation. *Journal of Geophysical Research: Space Physics*, 122, 765–779. <https://doi.org/10.1002/2016JA022645>
- Baumjohann, W., Georgescu, E., Fornaçon, K.-H., Auster, H. U., Treumann, R. A., & Haerendel, G. (2000). Magnetospheric lion roars. *Annales Geophysicae*, 18, 406–410. <https://doi.org/10.1007/s00585-000-0406-2>
- Baumjohann, W., Scokopke, N., LaBelle, J., Klecker, B., Lühr, H., & Glassmeier, K. H. (1987). Plasma and field observations of a compressional Pc 5 wave event. *Journal of Geophysical Research*, 92, 12203–12212. <https://doi.org/10.1029/JA092iA11p12203>
- Berchem, J., & Gendrin, R. (1985). Nonresonant interaction of heavy ions with electromagnetic ion cyclotron waves. *Journal of Geophysical Research*, 90, 10945–10960. <https://doi.org/10.1029/JA090iA11p10945>
- Blake, J. B., Mauk, B. H., Baker, D. N., Carranza, P., Clemmons, J. H., Craft, J., et al. (2016). The Fly's Eye Energetic Particle Spectrometer (FEEPS) sensors for the Magnetospheric Multiscale (MMS) mission. *Space Science Reviews*, 199, 309–329. <https://doi.org/10.1007/s11214-015-0163-x>
- Blum, L. W., MacDonald, E. A., Gary, S. P., Thomsen, M. F., & Spence, H. E. (2009). Ion observations from geosynchronous orbit as a proxy for ion cyclotron wave growth during storm times. *Journal of Geophysical Research*, 114, A10214. <https://doi.org/10.1029/2009JA014396>
- Breuillard, H., Le Contel, O., Chust, T., Berthomier, M., Retino, A., Turner, D. L., et al. (2018). The properties of lion roars and electron dynamics in mirror-mode waves observed by the Magnetospheric Multiscale mission. *Journal of Geophysical Research: Space Physics*, 123, 93–103. <https://doi.org/10.1002/2017JA024551>
- Burch, J. L., Moore, T. E., Torbert, R. B., & Giles, B. L. (2016). Magnetospheric multiscale overview and science objectives. *Space Science Reviews*, 199, 5–21. <https://doi.org/10.1007/s11214-015-0164-9>
- Chappell, C. R. (1974). Detached plasma regions in the magnetosphere. *Journal of Geophysical Research*, 79, 1861–1870. <https://doi.org/10.1029/JA079i013p01861>
- Chen, H., Gao, X., Lu, Q., & Wang, S. (2019). Analyzing EMIC waves in the inner magnetosphere using long-term Van Allen Probes observations. *Journal of Geophysical Research: Space Physics*, 124, 7402–7412. <https://doi.org/10.1029/2019JA026965>
- Chen, L., & Hasegawa, A. (1991). Kinetic theory of geomagnetic pulsations: 1. Internal excitations by energetic particles. *Journal of Geophysical Research*, 96(A2), 1503–1512. <https://doi.org/10.1029/90JA02346>
- Chen, L., Thorne, R. M., Jordanova, V. K., Wang, C.-P., Gkioulidou, M., Lyons, L., & Horne, R. B. (2010). Global simulation of EMIC wave excitation during the 21 April 2001 storm from coupled RCM-RAM-HOTRAY modeling. *Journal of Geophysical Research*, 115, A07209. <https://doi.org/10.1029/2009JA015075>
- Chen, S.-H., & Moore, T. (2006). Magnetospheric convection and thermal ions in the dayside outer magnetosphere. *Journal of Geophysical Research*, 111, A03215. <https://doi.org/10.1029/2005JA011084>
- Chen, C. H. K., Klein, K. G., & Howes, G. G. (2019). Evidence for electron Landau damping in space plasma turbulence. *Nature Communications*, 10, 740. <https://doi.org/10.1038/s41467-019-08435-3>
- Cheng, C. Z., & Lin, C. S. (1987). Eigenmode analysis of compressional waves in the magnetosphere. *Geophysical Research Letters*, 14, 884–887. <https://doi.org/10.1029/GL014i008p00884>
- Cheng, C. Z., & Qian, Q. (1994). Theory of ballooning-mirror instabilities for anisotropic pressure plasmas in the magnetosphere. *Journal of Geophysical Research*, 99(A6), 11193–11209. <https://doi.org/10.1029/94JA00657>
- Cho, J.-H., Lee, D.-Y., Noh, S.-J., Kim, H., Choi, C. R., Lee, J., & Hwang, J. (2017). Spatial dependence of electromagnetic ion cyclotron waves triggered by solar wind dynamic pressure enhancements. *Journal of Geophysical Research: Space Physics*, 122, 5502–5518. <https://doi.org/10.1002/2016JA023827>
- Cho, J.-H., Lee, D.-Y., Noh, S.-J., Shin, D.-K., Hwang, J., Kim, K.-C., et al. (2016). Van Allen Probes observations of electromagnetic ion cyclotron waves triggered by enhanced solar wind dynamic pressure. *Journal of Geophysical Research: Space Physics*, 121, 9771–9793. <https://doi.org/10.1002/2016JA022841>
- Constantinescu, O. D., Glassmeier, K. H., Plaschke, F., Auster, U., Angelopoulos, V., Baumjohann, W., et al. (2009). THEMIS observations of duskside compressional Pc5 waves. *Journal of Geophysical Research*, 114, A00C25. <https://doi.org/10.1029/2008JA013519>
- Cornwall, J. M. (1965). Cyclotron instabilities and electromagnetic emission in the ultra-low frequency and very low frequency ranges. *Journal of Geophysical Research*, 70, 61–69. <https://doi.org/10.1029/JZ070i001p00061>
- Cornwall, J. M., Coroniti, F. V., & Thorne, R. M. (1970). Turbulent loss of ring current protons. *Journal of Geophysical Research*, 75(25), 4699–4709. <https://doi.org/10.1029/JA075i025p04699>
- Darrouzet, F., De Keyser, J., Decreau, P. M. E., El Lemdani-Mazouz, F., & Vallières, X. (2008). Statistical analysis of plasmaspheric plumes with Cluster/WHISPER observations. *Annales Geophysicae*, 26(8), 2403–2417. <https://doi.org/10.5194/angeo-26-2403-2008>
- Denton, R. E., Anderson, B. J., Ho, G., & Hamilton, D. C. (1996). Effects of wave superposition on the polarization of electromagnetic ion cyclotron waves. *Journal of Geophysical Research*, 101(A11), 24869–24885. <https://doi.org/10.1029/96JA02251>
- Denton, R. E., Ofman, L., Shprits, Y. Y., Bortnik, J., Millan, R. M., Rodger, C. J., et al. (2019). Pitch angle scattering of sub-MeV relativistic electrons by electromagnetic ion cyclotron waves. *Journal of Geophysical Research: Space Physics*, 124, 5610–5626. <https://doi.org/10.1029/2018JA026384>
- Dubinin, E. M., Maksimovic, M., Cornilleau-Wehrlin, N., Fontaine, D., Travnicek, P., Mangeney, A., et al. (2007). Coherent whistler emissions in the magnetosphere: Cluster observations. *Annales Geophysicae*, 25, 303–315. <https://doi.org/10.5194/angeo-25-303-2007>
- Engelbreton, M. J., Posch, J. L., Capman, N. S. S., Campuzano, N. G., Bèlik, P., Allen, R. C., et al. (2018). MMS, Van Allen Probes, GOES 13, and ground-based magnetometer observations of EMIC wave events before, during, and after a modest interplanetary shock. *Journal of Geophysical Research: Space Physics*, 123, 8331–8357. <https://doi.org/10.1029/2018JA025984>
- Ergun, R. E., Carlson, C. W., McFadden, J. P., Clemmons, J. H., & Boehm, M. H. (1991). Langmuir wave growth and electron bunching: Results from a wave-particle correlator. *Journal of Geophysical Research*, 96(A1), 225–238. <https://doi.org/10.1029/90JA01596>
- Ergun, R. E., Carlson, C. W., McFadden, J. P., TonThat, D. M., Clemmons, J. H., & Boehm, M. H. (1991). Observation of electron bunching during Landau growth and damping. *Journal of Geophysical Research*, 96(A7), 11371–11378. <https://doi.org/10.1029/91JA00658>
- Ergun, R. E., Tucker, S., Westfall, J., Goodrich, K. A., Malaspina, D. M., Summers, D., et al. (2016). The axial double probe and fields signal processing for the MMS Mission. *Space Science Reviews*, 199, 167–188. <https://doi.org/10.1007/s11214-014-0115-x>

- Erlanson, R. E., & Ukhorskiy, A. J. (2001). Observations of electromagnetic ion cyclotron waves during geomagnetic storms: Wave occurrence and pitch angle scattering. *Journal of Geophysical Research*, *106*(A3), 3883–3895. <https://doi.org/10.1029/2000JA00083>
- Fadanelli, S., Lavraud, B., Califano, F., Jacquy, C., Vernisse, Y., Kacem, I., et al. (2019). Four-spacecraft measurements of the shape and dimensionality of magnetic structures in the near-Earth plasma environment. *Journal of Geophysical Research: Space Physics*, *124*, 6850–6868. <https://doi.org/10.1029/2019JA026747>
- Fok, M.-C., Khazanov, G. V., Krivorutsky, E. N., & Glocher, A. (2016). Convective growth of electromagnetic ion cyclotron waves from realistic ring current ion distributions. *Journal of Geophysical Research: Space Physics*, *121*, 10966–10977. <https://doi.org/10.1002/2016JA022964>
- Fraser, B. J., & Nguyen, T. S. (2001). Is the plasmapause a preferred source region of electromagnetic ion cyclotron waves in the magnetosphere? *Journal of Atmospheric and Solar-Terrestrial Physics*, *63*(11), 1225–1247. [https://doi.org/10.1016/s1364-6826\(00\)00225-x](https://doi.org/10.1016/s1364-6826(00)00225-x)
- Fu, X., Cowee, M. M., Jordanova, V. K., Gary, S. P., Reeves, G. D., & Winske, D. (2016). Predicting electromagnetic ion cyclotron wave amplitude from unstable ring current plasma conditions. *Journal of Geophysical Research: Space Physics*, *121*, 10954–10965. <https://doi.org/10.1002/2016JA023303>
- Fukuhara, H., Kojima, H., Ueda, Y., Omura, Y., Katoh, Y., & Yamanaka, H. (2009). A new instrument for the study of wave-particle interactions in space: One-chip wave-particle interaction analyzer. *Earth Planets and Space*, *61*, 765–778. <https://doi.org/10.1186/BF03353183>
- Fuselier, S. A., & Anderson, B. J. (1996). Low-energy He⁺ and H⁺ distributions and proton cyclotron waves in the afternoon equatorial magnetosphere. *Journal of Geophysical Research*, *101*(A6), 13255–13265. <https://doi.org/10.1029/96JA00292>
- Fuselier, S. A., Lewis, W. S., Schiff, C., Ergun, R., Burch, J. L., Petrinec, S. M., & Trattner, K. J. (2016). Magnetospheric Multiscale science emission profile and operations. *Space Science Reviews*, *199*, 77–103. <https://doi.org/10.1007/s11214-014-0087-x>
- Gary, S. P. (1992). The mirror and ion cyclotron anisotropy instabilities. *Journal of Geophysical Research*, *97*, 8519–8529. <https://doi.org/10.1029/92JA00299>
- Gary, S. P., Fu, X., Cowee, M. M., Winske, D., & Liu, K. (2017). Scalings for the Alfvén-cyclotron instability: Linear dispersion theory and hybrid particle-in-cell simulations. *Journal of Geophysical Research: Space Physics*, *122*, 464–474. <https://doi.org/10.1002/2016JA023425>
- Gary, S. P., Moldwin, M. B., Thomsen, M. F., Winske, D., & McComas, D. J. (1994). Hot proton anisotropies and cool proton temperatures in the outer magnetosphere. *Journal of Geophysical Research*, *99*(A12), 23603–23615. <https://doi.org/10.1029/94JA02069>
- Génot, V., Budnik, E., Hellinger, P., Passot, T., Belmont, G., Trávníček, P. M., et al. (2009). Mirror structures above and below the linear instability threshold: Cluster observations, fluid model and hybrid simulations. *Annales Geophysicae*, *27*(2), 601–615. <https://doi.org/10.5194/angeo-27-601-2009>
- Gershman, D. J., Avanon, L. A., Boardsen, S. A., Dorelli, J. C., Gliese, U., Barrie, A. C., et al. (2017). Spacecraft and instrument photoelectrons measured by the dual electron spectrometers on MMS. *Journal of Geophysical Research: Space Physics*, *122*, 11548–11558. <https://doi.org/10.1002/2017JA024518>
- Gershman, D. J., F-Viñas, A., Dorelli, J. C., Boardsen, S. A., Avanon, L. A., Bellan, P. M., et al. (2017). Wave-particle energy exchange directly observed in a kinetic Alfvén-branch wave. *Nature Communications*, *8*, 14719. <https://doi.org/10.1038/ncomms14719>
- Halford, A. J., Fraser, B. J., & Morley, S. K. (2015). EMIC waves and plasmaspheric and plume density: CRRES results. *Journal of Geophysical Research: Space Physics*, *120*, 1974–1992. <https://doi.org/10.1002/2014JA020338>
- Hasegawa, A. (1969). Drift mirror instability in the magnetosphere. *Physics of Fluids*, *12*, 2642–2650. <https://doi.org/10.1063/1.1692407>
- He, J., Duan, D., Wang, T., Zhu, X., Li, W. Y., Verscharen, D., et al. (2019). Direct measurement of the dissipation rate spectrum around ion kinetic scales in space plasma turbulence. *The Astrophysical Journal*, *880*(2), 121. <https://doi.org/10.3847/1538-4357/ab2a79>
- He, J., Zhu, X., Verscharen, D., Duan, D., Zhao, J., & Wang, T. (2020). Spectra of diffusion, dispersion, and dissipation for kinetic Alfvénic and compressive turbulence: Comparison between kinetic theory and measurements from MMS. *The Astrophysical Journal*, *898*(1), 43. <https://doi.org/10.3847/1538-4357/ab9174>
- Horne, R. B., & Thorne, R. M. (1993). On the preferred source location for the convective amplification of ion cyclotron waves. *Journal of Geophysical Research*, *98*(A6), 9233–9247. <https://doi.org/10.1029/92JA02972>
- Howes, G. G., Klein, K. G., & Li, T. C. (2017). Diagnosing collisionless energy transfer using field-particle correlations: Vlasov-Poisson plasmas. *Journal of Plasma Physics*, *83*(1), 705830102. <https://doi.org/10.1017/S0022377816001197>
- Hsieh, Y.-K., & Omura, Y. (2017). Nonlinear dynamics of electrons interacting with oblique whistler mode chorus in the magnetosphere. *Journal of Geophysical Research: Space Physics*, *122*, 675–694. <https://doi.org/10.1002/2016JA023255>
- Hsieh, Y.-K., & Omura, Y. (2018). Nonlinear damping of oblique whistler mode waves via Landau resonance. *Journal of Geophysical Research: Space Physics*, *123*, 7462–7472. <https://doi.org/10.1029/2018JA025848>
- Hubert, D., Lacombe, C., Harvey, C. C., Moncuquet, M., Russell, C. T., & Thomsen, M. F. (1998). Nature, properties, and origin of low frequency waves from an oblique shock to the inner magnetosheath. *Journal of Geophysical Research*, *103*, 26783–26798. <https://doi.org/10.1029/98JA01011>
- Hull, A. J., Muschietti, L., Le Contel, O., Dorelli, J. C., & Lindqvist, P.-A. (2020). MMS observations of intense whistler waves within Earth's supercritical bow shock: Source mechanism and impact on shock structure and plasma transport. *Journal of Geophysical Research: Space Physics*, *125*, e2019JA027290. <https://doi.org/10.1029/2019JA027290>
- Jordanova, V. K., Farrugia, C. J., Thorne, R. M., Khazanov, G. V., Reeves, G. D., & Thomsen, M. F. (2001). Modeling ring current proton precipitation by electromagnetic ion cyclotron waves during the May 14–16, 1997, storm. *Journal of Geophysical Research*, *106*(A1), 7–22. <https://doi.org/10.1029/2000JA002008>
- Jordanova, V. K., Spasojevic, M., & Thomsen, M. F. (2007). Modeling the electromagnetic ion cyclotron wave-induced formation of detached subauroral proton arcs. *Journal of Geophysical Research*, *112*, A08209. <https://doi.org/10.1029/2006JA012215>
- Jun, C.-W., Yue, C., Bortnik, J., Lyons, L. R., Nishimura, Y. T., Kletzing, C. A., et al. (2019). A statistical study of EMIC waves associated with and without energetic particle injection from the magnetotail. *Journal of Geophysical Research: Space Physics*, *124*, 433–450. <https://doi.org/10.1029/2018JA025886>
- Kakad, A., Kakad, B., Omura, Y., Sinha, A. K., Upadhyay, A., & Rawat, R. (2019). Modulation of electromagnetic ion cyclotron waves by Pc5 ULF waves and energetic ring current ions. *Journal of Geophysical Research: Space Physics*, *124*, 1992–2009. <https://doi.org/10.1029/2017JA024930>
- Katoh, Y., Kitahara, M., Kojima, H., Omura, Y., Kasahara, S., Hirahara, M., et al. (2013). Significance of wave-particle interaction analyzer for direct measurements of nonlinear wave-particle interactions. *Annales Geophysicae*, *31*, 503–512. <https://doi.org/10.5194/angeo-31-503-2013>
- Katoh, Y., Kojima, H., Hikishima, M., Takashima, T., Asamura, K., Miyoshi, Y., et al. (2018). Software-type wave-particle interaction analyzer on board the Arase satellite. *Earth Planets and Space*, *70*, 4. <https://doi.org/10.1186/s40623-017-0771-7>
- Keika, K., Takahashi, K., Ukhorskiy, A. Y., & Miyoshi, Y. (2013). Global characteristics of electromagnetic ion cyclotron waves: Occurrence rate and its storm dependence. *Journal of Geophysical Research: Space Physics*, *118*, 4135–4150. <https://doi.org/10.1002/jgra.50385>

- Kennel, C. F., & Petschek, H. E. (1966). Limit on stably trapped particle fluxes. *Journal of Geophysical Research*, 71, 1–28. <https://doi.org/10.1029/JZ071i001p00001>
- Kim, G.-J., Kim, K.-H., Lee, D.-H., Kwon, H.-J., & Park, J.-S. (2016). Occurrence of EMIC waves and plasmaspheric plasmas derived from THEMIS observations in the outer magnetosphere: Revisit. *Journal of Geophysical Research: Space Physics*, 121, 9443–9458. <https://doi.org/10.1002/2016JA023108>
- Kim, K. H., Omura, Y., Jin, H., & Hwang, J. (2017). A case study of EMIC waves associated with sudden geosynchronous magnetic field changes. *Journal of Geophysical Research: Space Physics*, 122, 3322–3341. <https://doi.org/10.1002/2016JA023391>
- Kitahara, M., & Katoh, Y. (2016). Method for direct detection of pitch angle scattering of energetic electrons caused by whistler mode chorus emissions. *Journal of Geophysical Research: Space Physics*, 121, 5137–5148. <https://doi.org/10.1002/2015JA021902>
- Kitamura, N., Kitahara, M., Shoji, M., Miyoshi, Y., Hasegawa, H., Nakamura, S., et al. (2018). Direct measurements of two-way wave-particle energy transfer in a collisionless space plasma. *Science*, 361(6406), 1000–1003. <https://doi.org/10.1126/science.aap8730>
- Kitamura, N., Omura, Y., Nakamura, S., Amano, T., Boardsen, S. A., Ahmadi, N., et al. (2020). Observations of the source region of whistler mode waves in magnetosheath mirror structures. *Journal of Geophysical Research: Space Physics*, 125, e2019JA027488. <https://doi.org/10.1029/2019JA027488>
- Kivelson, M. G., & Southwood, D. J. (1996). Mirror instability II: The mechanism of nonlinear saturation. *Journal of Geophysical Research*, 101(A8), 17365–17371. <https://doi.org/10.1029/96JA01407>
- Klein, K. G., Howes, G. G., & TenBarge, J. M. (2017). Diagnosing collisionless energy transfer using field-particle correlations: Gyrokinetic turbulence. *Journal of Plasma Physics*, 83(4), 535830401. <https://doi.org/10.1017/S0022377817000563>
- Kletzing, C. A., Bounds, S. R., LaBelle, J., & Samara, M. (2005). Observation of the reactive component of Langmuir wave phase-bunched electrons. *Geophysical Research Letters*, 32, L05106. <https://doi.org/10.1029/2004GL021175>
- Kletzing, C. A., LaBelle, J., Bounds, S. R., Dolan, J., Kaeppler, S. R., & Dombrowski, M. (2017). Phase sorting wave-particle correlator. *Journal of Geophysical Research: Space Physics*, 122, 2069–2078. <https://doi.org/10.1002/2016JA023334>
- Korotova, G. I., Sibeck, D. G., Angelopoulos, V., & Walsh, B. M. (2013). THEMIS observations of compressional poloidal pulsations in the dawnside magnetosphere: A case study. *Journal of Geophysical Research: Space Physics*, 118, 7665–7673. <https://doi.org/10.1002/2013JA019360>
- Korotova, G. I., Sibeck, D. G., Kondratovich, V., Angelopoulos, V., & Constantinescu, O. D. (2009). Themis observations of compressional pulsations in the dawn-side magnetosphere, a case study. *Annales Geophysicae*, 27, 1–11. <https://doi.org/10.5194/angeo-27-3725-2009>
- Kozyra, J. U., Cravens, T. E., Nagy, A. F., Fonthelm, E. G., & Ong, R. S. B. (1984). Effects of energetic heavy ions on electromagnetic ion cyclotron wave generation in the plasmopause region. *Journal of Geophysical Research*, 89, 2217–2233. <https://doi.org/10.1029/JA089iA04p02217>
- Kozyra, J. U., Jordanova, V. K., Home, R. B., & Thorne, R. M. (1997). Modeling of the contribution of electromagnetic ion cyclotron (EMIC) waves to stormtime ring current erosion. *Magnetic Storms, Geophysical Monograph*, 98, 187–202. <https://doi.org/10.1029/GM098p0187>
- Kubota, Y., & Omura, Y. (2017). Rapid precipitation of radiation belt electrons induced by EMIC rising tone emissions localized in longitude inside and outside the plasmopause. *Journal of Geophysical Research: Space Physics*, 122, 293–309. <https://doi.org/10.1002/2016JA023267>
- Kurita, S., Miyoshi, Y., Shiokawa, K., Higashio, N., Mitani, T., Takashima, T., et al. (2018). Rapid loss of relativistic electrons by EMIC waves in the outer radiation belt observed by Arase, Van Allen Probes, and the PWING ground stations. *Geophysical Research Letters*, 45, 12720–12729. <https://doi.org/10.1029/2018GL080262>
- Kwon, H.-J., Kim, K.-H., Jee, G., Park, J.-S., Jin, H., & Nishimura, Y. (2015). Plasmopause location under quiet geomagnetic conditions ($K_p \leq 1$): THEMIS observations. *Geophysical Research Letters*, 42, 7303–7310. <https://doi.org/10.1002/2015GL066090>
- Lanzerotti, L. J., Hasegawa, A., & MacLennan, C. G. (1969). Drift mirror instability in the magnetosphere: Particle and field oscillations and electron heating. *Journal of Geophysical Research*, 74(24), 5565–5578. <https://doi.org/10.1029/JA074i024p05565>
- Lee, J., Min, K., & Kim, K.-S. (2013). Characteristic dimension of electromagnetic ion cyclotron wave activity in the magnetosphere. *Journal of Geophysical Research: Space Physics*, 118, 1651–1658. <https://doi.org/10.1002/jgra.50242>
- Lee, J. H., & Angelopoulos, V. (2014). On the presence and properties of cold ions near Earth's equatorial magnetosphere. *Journal of Geophysical Research: Space Physics*, 119, 1749–1770. <https://doi.org/10.1002/2013JA019305>
- Lee, J. H., Turner, D. L., Toledo-Redondo, S., Vines, S. K., Allen, R. C., Fuselier, S. A., et al. (2019). MMS measurements and modeling of peculiar electromagnetic ion cyclotron waves. *Geophysical Research Letters*, 46, 11622–11631. <https://doi.org/10.1029/2019GL085182>
- Lee, S. H., Zhang, H., Zong, Q.-G., Otto, A., Rème, H., & Liebert, E. (2016). A statistical study of plasmaspheric plumes and ionospheric outflows observed at the dayside magnetopause. *Journal of Geophysical Research: Space Physics*, 121, 492–506. <https://doi.org/10.1002/2015JA021540>
- Li, T. C., Howes, G. G., Klein, K. G., Liu, Y.-H., & TenBarge, J. M. (2019). Collisionless energy transfer in kinetic turbulence: field-particle correlations in Fourier space. *Journal of Plasma Physics*, 85(4), 905850406. <https://doi.org/10.1017/S0022377819000515>
- Li, W., Thorne, R. M., Bortnik, J., Nishimura, Y., & Angelopoulos, V. (2011). Modulation of whistler mode chorus waves: 1. Role of compressional Pc4–5 pulsations. *Journal of Geophysical Research*, 116, A06205. <https://doi.org/10.1029/2010JA016312>
- Lin, N., McPherron, R. L., Kivelson, M. G., & Williams, D. J. (1988). An unambiguous determination of the propagation of a compressional Pc 5 wave. *Journal of Geophysical Research*, 93, 5601–5612. <https://doi.org/10.1029/JA093iA06p05601>
- Lin, R.-L., Zhang, J.-C., Allen, R. C., Kistler, L. M., Mouikis, C. G., Gong, J.-C., et al. (2014). Testing linear theory of EMIC waves in the inner magnetosphere: Cluster observations. *Journal of Geophysical Research: Space Physics*, 119, 1004–1027. <https://doi.org/10.1002/2013JA019541>
- Lindqvist, P.-A., Olsson, G., Torbert, R. B., King, B., Granoff, M., Rau, D., et al. (2016). The spin-plane double probe electric field instrument for MMS. *Space Science Reviews*, 199, 137–165. <https://doi.org/10.1007/s11214-014-0116-9>
- Liu, S., Xia, Z., Chen, L., Liu, Y., Liao, Z., & Zhu, H. (2019). Magnetospheric Multiscale Observation of quasiperiodic EMIC waves associated with enhanced solar wind pressure. *Geophysical Research Letters*, 46, 7096–7104. <https://doi.org/10.1029/2019GL083421>
- Liu, Y. H., Fraser, B. J., & Menk, F. W. (2012). Pc2 EMIC waves generated high off the equator in the dayside outer magnetosphere. *Geophysical Research Letters*, 39, L17102. <https://doi.org/10.1029/2012GL053082>
- Loto'aniu, T., Fraser, B., & Waters, C. (2009). The modulation of electromagnetic ion cyclotron waves by Pc 5 ULF waves. *Annales Geophysicae*, 27, 121–130. <https://doi.org/10.5194/angeo-27-121-2009>
- Loto'aniu, T. M., Fraser, B. J., & Waters, C. L. (2005). Propagation of electromagnetic ion cyclotron wave energy in the magnetosphere. *Journal of Geophysical Research*, 110, A07214. <https://doi.org/10.1029/2004JA010816>
- Lyons, L. R., & Thorne, R. M. (1972). Parasitic pitch angle diffusion of radiation belt particles by ion cyclotron waves. *Journal of Geophysical Research*, 77(28), 5608–5616. <https://doi.org/10.1029/JA077i028p05608>

- Ma, Q., Li, W., Yue, C., Thorne, R. M., Bortnik, J., Kletzing, C. A., et al. (2019). Ion heating by electromagnetic ion cyclotron waves and magnetosonic waves in the Earth's inner magnetosphere. *Geophysical Research Letters*, *46*, 6258–6267. <https://doi.org/10.1029/2019GL083513>
- Maksimovic, M., Harvey, C. C., Santolik, O., Lacombe, C., de Conchy, Y., Hubert, D., et al. (2001). Polarisation and propagation of lion roars in the dusk side magnetosheath. *Annales Geophysicae*, *19*, 1429–1438. <https://doi.org/10.5194/angeo-19-1429-2001>
- Matsuda, S., Kasahara, Y., Miyoshi, Y., Nomura, R., Shoji, M., Matsuoka, A., et al. (2018). Spatial distribution of fine-structured and unstructured EMIC waves observed by the Arase satellite. *Geophysical Research Letters*, *45*, 11530–11538. <https://doi.org/10.1029/2018GL080109>
- Mauk, B. H., Blake, J. B., Baker, D. N., Clemmons, J. H., Reeves, G. D., Spence, H. E., et al. (2016). The Energetic particle detector (EPD) investigation and the energetic ion spectrometer (EIS) for the Magnetospheric Multiscale (MMS) mission. *Space Science Reviews*, *199*, 471–514. <https://doi.org/10.1007/s11214-014-0055-5>
- Mauk, B. H., McIlwain, C. E., & McPherron, R. L. (1981). Helium cyclotron resonance within the Earth's magnetosphere. *Geophysical Research Letters*, *8*(1), 103–106. <https://doi.org/10.1029/GL008i001p00103>
- Meredith, N. P., Horne, R. B., Kersten, T., Fraser, B. J., & Grew, R. S. (2014). Global morphology and spectral properties of EMIC waves derived from CRRES observations. *Journal of Geophysical Research: Space Physics*, *119*, 5328–5342. <https://doi.org/10.1002/2014JA020064>
- Min, K., Lee, J., Keika, K., & Li, W. (2012). Global distribution of EMIC waves derived from THEMIS observations. *Journal of Geophysical Research*, *117*, A05219. <https://doi.org/10.1029/2012JA017515>
- Miyoshi, Y., Sakaguchi, K., Shiokawa, K., Evans, D., Albert, J., Connors, M., & Jordanova, V. (2008). Precipitation of radiation belt electrons by EMIC waves, observed from ground and space. *Geophysical Research Letters*, *35*, L23101. <https://doi.org/10.1029/2008GL035727>
- Mourenas, D., Artemyev, A. V., Ma, Q., Agapitov, O. V., & Li, W. (2016). Fast dropouts of multi-MeV electrons due to combined effects of EMIC and whistler mode waves. *Geophysical Research Letters*, *43*, 4155–4163. <https://doi.org/10.1002/2016GL068921>
- Mursula, K., Brys, T., Niskala, K., & Russell, C. T. (2001). Pc1 pearls revisited: Structured electromagnetic ion cyclotron waves on Polar satellite and on ground. *Journal of Geophysical Research*, *106*(A12), 29543–29553. <https://doi.org/10.1029/2000JA003044>
- Nakamura, S., Omura, Y., & Angelopoulos, V. (2016). A statistical study of EMIC rising and falling tone emissions observed by THEMIS. *Journal of Geophysical Research: Space Physics*, *121*, 8374–8391. <https://doi.org/10.1002/2016JA022353>
- Nakamura, S., Omura, Y., Kletzing, C., & Baker, D. N. (2019). Rapid precipitation of relativistic electron by EMIC rising-tone emissions observed by the Van Allen Probes. *Journal of Geophysical Research: Space Physics*, *124*, 6701–6714. <https://doi.org/10.1029/2019JA026772>
- Nishi, K., Shiokawa, K., Glassmeier, K.-H., & Mieth, J. Z. D. (2018). Statistical study of phase relationship between magnetic and plasma pressures in the near-Earth nightside magnetosphere using the THEMIS-E satellite. *Journal of Geophysical Research: Space Physics*, *123*, 9517–9531. <https://doi.org/10.1029/2018JA025846>
- Noh, S.-J., Lee, D.-Y., Choi, C.-R., Kim, H., & Skoug, R. (2018). Test of ion cyclotron resonance instability using proton distributions obtained from Van Allen Probe-A observations. *Journal of Geophysical Research: Space Physics*, *123*, 6591–6610. <https://doi.org/10.1029/2018JA025385>
- Ofman, L., Denton, R. E., Bortnik, J., An, X., Glocer, A., & Komar, C. (2017). Growth and nonlinear saturation of electromagnetic ion cyclotron waves in multi-ion species magnetospheric plasma. *Journal of Geophysical Research: Space Physics*, *122*, 6469–6484. <https://doi.org/10.1002/2017ja024172>
- Omura, Y., Ashour-Abdalla, M., Gendrin, R., & Quest, K. (1985). Heating of thermal helium in the equatorial magnetosphere: A simulation study. *Journal of Geophysical Research*, *90*(A9), 8281–8390. <https://doi.org/10.1029/JA090iA09p08281>
- Omura, Y., Hsieh, Y.-K., Foster, J. C., Erickson, P. J., Kletzing, C. A., & Baker, D. N. (2019). Cyclotron acceleration of relativistic electrons through Landau resonance with obliquely propagating whistler-mode chorus emissions. *Journal of Geophysical Research: Space Physics*, *124*, 2795–2810. <https://doi.org/10.1029/2018JA026374>
- Omura, Y., Katoh, Y., & Summers, D. (2008). Theory and simulation of the generation of whistler-mode chorus. *Journal of Geophysical Research*, *113*, A04223. <https://doi.org/10.1029/2007JA012622>
- Omura, Y., Pickett, J., Grison, B., Santolik, O., Dandouras, I., Engebretson, M., et al. (2010). Theory and observation of electromagnetic ion cyclotron triggered emissions in the magnetosphere. *Journal of Geophysical Research*, *115*, A07234. <https://doi.org/10.1029/2010JA015300>
- Ozaki, M., Shiokawa, K., Miyoshi, Y., Kataoka, R., Connors, M., Inoue, T., et al. (2018). Discovery of 1 Hz range modulation of isolated proton aurora at subauroral latitudes. *Geophysical Research Letters*, *45*, 1209–1217. <https://doi.org/10.1002/2017GL076486>
- Pakhotin, I. P., Walker, S. N., Shprits, Y. Y., & Balikhin, M. A. (2013). Dispersion relation of electromagnetic ion cyclotron waves using Cluster observations. *Annales Geophysicae*, *31*(8), 1437–1446. <https://doi.org/10.5194/angeo-31-1437-2013>
- Plyasova-Bakounina, T. A., Kangas, J., Mursula, K., Molchanov, O. A., & Green, A. W. (1996). Pc 1-2 and Pc 4-5 pulsations observed at a network of high-latitude stations. *Journal of Geophysical Research*, *101*(A5), 10965–10973. <https://doi.org/10.1029/95JA03770>
- Pollock, C., Moore, T., Jacques, A., Burch, J., Gliese, U., Saito, Y., et al. (2016). Fast plasma investigation for magnetospheric multiscale. *Space Science Reviews*, *199*, 331–406. <https://doi.org/10.1007/s11214-016-0245-4>
- Rae, I. J., Mann, I. R., Watt, C. E. J., Kistler, L. M., & Baumjohann, W. (2007). Equator-S observations of drift mirror mode waves in the dawnside magnetosphere. *Journal of Geophysical Research*, *112*, A11203. <https://doi.org/10.1029/2006JA012064>
- Rasinkangas, R., & Mursula, K. (1998). Modulation of magnetospheric EMIC waves by Pc 3 pulsations of upstream origin. *Geophysical Research Letters*, *25*(6), 869–872. <https://doi.org/10.1029/98GL50415>
- Rasinkangas, R., Mursula, K., Kremser, G., Singer, H., Fraser, B., Korth, A., & Hughes, W. (1994). Simultaneous occurrence of Pc 5 and Pc 1 pulsations in the dawnside magnetosphere: CRRES observations. Solar Wind Sources of Magnetospheric Ultra-Low-Frequency Waves. *Geophysical Monograph*, *81*, 417–424. <https://doi.org/10.1029/GM081p0417>
- Roux, A., Perraut, S., Rauch, J. L., de Villedary, C., Kremser, G., Korth, A., & Young, D. T. (1982). Wave-particle interactions near Ω_{He^+} observed on board GEOS 1 and 2: 2. Generation of ion cyclotron waves and heating of He^+ ions. *Journal of Geophysical Research*, *87*, 8174–8190. <https://doi.org/10.1029/JA087iA10p08174>
- Russell, C. T., Anderson, B. J., Baumjohann, W., Bromund, K. R., Dearborn, D., Fischer, D., et al. (2016). The magnetospheric multiscale magnetometers. *Space Science Reviews*, *199*, 189–256. <https://doi.org/10.1007/s11214-014-0057-3>
- Saikin, A. A., Jordanova, V. K., Zhang, J. C., Smith, C. W., Spence, H. E., Larsen, B. A., & Shprits, Y. Y. (2018). Comparing simulated and observed EMIC wave amplitudes using in situ Van Allen Probes' measurements. *Journal of Atmospheric and Terrestrial Physics*, *177*, 190–201. <https://doi.org/10.1016/j.jastp.2018.01.024>
- Saikin, A. A., Zhang, J.-C., Smith, C. W., Spence, H. E., Torbert, R. B., & Kletzing, C. A. (2016). The dependence on geomagnetic conditions and solar wind dynamic pressure of the spatial distributions of EMIC waves observed by the Van Allen Probes. *Journal of Geophysical Research: Space Physics*, *121*, 4362–4377. <https://doi.org/10.1002/2016JA022523>
- Sakaguchi, K., Shiokawa, K., Miyoshi, Y., Otsuka, Y., Ogawa, T., Asamura, K., & Connors, M. (2008). Simultaneous appearance of isolated auroral arcs and Pc 1 geomagnetic pulsations at subauroral latitudes. *Journal of Geophysical Research*, *113*, A05201. <https://doi.org/10.1029/2007JA012888>

- Schwartz, S. J. (1998). Shock and discontinuity normals, mach numbers, and related parameters. In G. Paschmann, & P. W. Daly (Eds.), *Analysis methods for multispacecraft data* (pp. 249–270). Noordwijk, Netherlands. European Space Agency Publication.
- Shklyar, D., & Matsumoto, H. (2009). Oblique whistler-mode waves in the inhomogeneous magnetospheric plasma: Resonant interactions with energetic charged particles. *Surveys in Geophysics*, 30, 55–104. <https://doi.org/10.1007/s10712-009-9061-7>
- Shoji, M., Miyoshi, Y., Katoh, Y., Keika, K., Angelopoulos, V., Kasahara, et al. (2017). Ion hole formation and nonlinear generation of electromagnetic ion cyclotron waves: THEMIS observations. *Geophysical Research Letters*, 44, 8730–8738. <https://doi.org/10.1002/2017GL074254>
- Shoji, M., & Omura, Y. (2014). Spectrum characteristics of electromagnetic ion cyclotron triggered emissions and associated energetic proton dynamics. *Journal of Geophysical Research: Space Physics*, 119, 3480–3489. <https://doi.org/10.1002/2013JA019695>
- Shoji, M., Omura, Y., Tsurutani, B. T., Verkhoglyadova, O. P., & Lembège, B. (2009). Mirror instability and L-mode electromagnetic ion cyclotron instability: Competition in the Earth's magnetosheath. *Journal of Geophysical Research*, 114, A10203. <https://doi.org/10.1029/2008JA014038>
- Smith, E. J., Holtzer, R. E., & Russell, C. T. (1969). Magnetic emissions in the magnetosheath at frequencies near 100 Hz. *Journal of Geophysical Research*, 74, 3027–3036. <https://doi.org/10.1029/JA074i011p03027>
- Smith, E. J., & Tsurutani, B. T. (1976). Magnetosheath lion roars. *Journal of Geophysical Research*, 81, 2261–2266. <https://doi.org/10.1029/JA081i013p02261>
- Soto-Chavez, A. R., Lanzerotti, L. J., Manweiler, J. W., Gerrard, A., Cohen, R., Xia, Z., et al. (2019). Observational evidence of the drift-mirror plasma instability in Earth's inner magnetosphere. *Physics of Plasmas*, 26(4), 042110. <https://doi.org/10.1063/1.5083629>
- Soucek, J., & Escoubert, C. P. (2011). Cluster observations of trapped ions interacting with magnetosheath mirror modes. *Annales Geophysicae*, 29(6), 1049–1060. <https://doi.org/10.5194/angeo-29-1049-2011>
- Soucek, J., Lucek, E., & Dandouras, I. (2008). Properties of magnetosheath mirror modes observed by Cluster and their response to changes in plasmameters. *Journal of Geophysical Research*, 113, A04203. <https://doi.org/10.1029/2007JA012649>
- Su, S.-Y., Konradi, A., & Fritz, T. A. (1977). On propagation direction of ring current proton ULF waves observed by ATS 6 at 6.6 Re. *Journal of Geophysical Research*, 82, 1859–1868. <https://doi.org/10.1029/JA082i013p01859>
- Summers, D., & Thorne, R. M. (2003). Relativistic electron pitch-angle scattering by electromagnetic ion cyclotron waves during geomagnetic storms. *Journal of Geophysical Research*, 108(A4), 1143. <https://doi.org/10.1029/2002JA009489>
- Takahashi, K., Fennell, J. F., Amata, E., & Higbie, P. R. (1987). Field-aligned structure of the storm time Pc 5 wave of November 14–15. *Journal of Geophysical Research*, 92, 5857–5864. <https://doi.org/10.1029/JA092iA06p05857>
- Takahashi, K., Lopez, R. E., McEntire, R. W., Zanetti, L. J., Kistler, L. M., & Ipavich, F. M. (1987). An eastward propagating compressional Pc 5 wave observed by AMPTE/CCE in the postmidnight sector. *Journal of Geophysical Research*, 92, 13472–13484. <https://doi.org/10.1029/JA092iA12p13472>
- Tenerani, A., Le Contel, O., Califano, F., Robert, P., Fontaine, D., Cornilleau-Wehrlin, N., & Sauvaud, J.-A. (2013). Cluster observations of whistler waves correlated with ion-scale magnetic structures during the 17 August 2003 substorm event. *Journal of Geophysical Research: Space Physics*, 118, 6072–6089. <https://doi.org/10.1002/jgra.50562>
- Tetrick, S., Engebretson, M., Posch, J., Olson, C., Smith, C., Denton, R., et al. (2017). Location of intense electromagnetic ion cyclotron (EMIC) wave events relative to the plasmopause: Van Allen Probes observations. *Journal of Geophysical Research: Space Physics*, 122, 4064–4088. <https://doi.org/10.1002/2016JA023392>
- Thébault, E., Finlay, C. C., Beggan, C. D., Alken, P., Aubert, J., Barrois, O., et al. (2015). International Geomagnetic Reference Field: The 12th generation. *Earth Planets and Space*, 67, 79. <https://doi.org/10.1186/s40623-015-0228-9>
- Thorne, R. M., & Kennel, C. F. (1971). Relativistic electron precipitation during magnetic storm main phase. *Journal of Geophysical Research*, 76, 4446–4453. <https://doi.org/10.1029/JA076i019p04446>
- Tian, A., Xiao, K., Degeling, A. W., Shi, Q. Q., Park, J.-S., Nowada, M., & Pitkänen, T. (2020). Reconstruction of plasma structure with anisotropic pressure: Application to Pc5 compressional wave. *The Astrophysical Journal*, 889(1), 35. <https://doi.org/10.3847/1538-4357/ab6296>
- Torbert, R. B., Russell, C. T., Magnes, W., Ergun, R. E., Lindqvist, P. A., Le Contel, O., et al. (2016). The FIELDS instrument suite on MMS: Scientific objectives, measurements, and data products. *Space Science Reviews*, 199, 105–135. <https://doi.org/10.1007/s11214-014-0109-8>
- Torkar, K., Nakamura, R., Tajmar, M., Scharlemann, C., Jeszenszky, H., Laky, G., et al. (2016). Active spacecraft potential control investigation. *Space Science Reviews*, 199, 515–544. <https://doi.org/10.1007/s11214-014-0049-3>
- Torkar, K., Nakamura, R., Wellenzohn, S., Jeszenszky, H., Torbert, R. B., Lindqvist, P.-A., et al. (2019). Improved determination of plasma density based on spacecraft potential of the Magnetospheric Multiscale mission under active potential control. *IEEE Transactions on Plasma Science*, 47(8), 3636–3647. <https://doi.org/10.1109/TPS.2019.2911425>
- Tsyganenko, N. A., & Stern, D. P. (1996). Modeling the global magnetic field of the large-scale Birkeland current systems. *Journal of Geophysical Research*, 101(A12), 27187–27198. <https://doi.org/10.1029/96JA02735>
- Usanova, M. E., Darrouzet, F., Mann, I. R., & Bortnik, J. (2013). Statistical analysis of EMIC waves in plasmaspheric plumes from Cluster observations. *Journal of Geophysical Research: Space Physics*, 118, 4946–4951. <https://doi.org/10.1002/jgra.50464>
- Usanova, M. E., Mann, I. R., Bortnik, J., Shao, L., & Angelopoulos, V. (2012). THEMIS observations of electromagnetic ion cyclotron wave occurrence: Dependence on AE, SYM-H, and solar wind dynamic pressure. *Journal of Geophysical Research*, 117, A10218. <https://doi.org/10.1029/2012JA018049>
- Vaivads, A., Baumjohann, W., Haerendel, G., Nakamura, R., Kucharek, H., Klecker, B., et al. (2001). Compressional Pc5 type pulsations in the morningside plasma sheet. *Annales Geophysicae*, 19(3), 311–320. <https://doi.org/10.5194/angeo-19-311-2001>
- Vines, S. K., Allen, R. C., Anderson, B. J., Engebretson, M. J., Fuselier, S. A., Russell, C. T., et al. (2019). EMIC waves in the outer magnetosphere: Observations of an off-equator source region. *Geophysical Research Letters*, 46, 5707–5716. <https://doi.org/10.1029/2019GL082152>
- Walker, S. N., & Moiseenko, I. (2013). Determination of wave vectors using the phase differencing method. *Annales Geophysicae*, 31, 1611–1617. <https://doi.org/10.5194/angeo-31-1611-2013>
- Walsh, B. M., Sibeck, D. G., Nishimura, Y., & Angelopoulos, V. (2013). Statistical analysis of the plasmaspheric plume at the magnetopause. *Journal of Geophysical Research: Space Physics*, 118, 4844–4851. <https://doi.org/10.1002/jgra.50458>
- Wang, B., Li, P., Huang, J., & Zhang, B. (2019). Nonlinear Landau resonance between EMIC waves and cold electrons in the inner magnetosphere. *Physics of Plasmas*, 26(4), 042903. <https://doi.org/10.1063/1.5088374>
- Wang, X. Y., Huang, S. Y., Allen, R. C., Fu, H. S., Deng, X. H., Zhou, M., et al. (2017). The occurrence and wave properties of EMIC waves observed by the Magnetospheric Multiscale (MMS) mission. *Journal of Geophysical Research: Space Physics*, 122, 8228–8240. <https://doi.org/10.1002/2017JA024237>

- Xia, Z., Chen, L., Dai, L., Claudepierre, S. G., Chan, A. A., Soto-Chavez, A. R., & Reeves, G. D. (2016). Modulation of chorus intensity by ULF waves deep in the inner magnetosphere. *Geophysical Research Letters*, *43*, 9444–9452. <https://doi.org/10.1002/2016GL070280>
- Yahnina, T. A., Yahnin, A. G., Kangas, J., & Manninen, J. (2000). Proton precipitation related to Pc1 pulsations. *Geophysical Research Letters*, *27*(21), 3575–3578. <https://doi.org/10.1029/2000GL003763>
- Yokota, S., Kasahara, S., Mitani, T., Asamura, K., Hirahara, M., Takashima, T., et al. (2017). Medium-energy particle experiments-ion mass analyzer (MEP-i) onboard ERG (Arase). *Earth Planets and Space*, *69*(1), 172. <https://doi.org/10.1186/s40623-017-0754-8>
- Young, D. T., Burch, J. L., Gomez, R. G., Los Santos, A., Miller, G. P., Wilson, P. I. V., et al. (2016). Hot plasma composition analyzer for the Magnetospheric Multiscale mission. *Space Science Reviews*, *199*, 407–470. <https://doi.org/10.1007/s11214-014-0119-6>
- Young, D. T., Perraut, S., Roux, A., de Villedary, C., Gendrin, R., Korth, A., et al. (1981). Wave-particle interactions near Ω_{He^+} observed on GEOS 1 and 2. I - Propagation of ion cyclotron waves in He^+ -rich plasma. *Journal of Geophysical Research*, *86*, 6755–6772. <https://doi.org/10.1029/JA086iA08p06755>
- Yuan, Z., Xiong, Y., Huang, S., Deng, X., Pang, Y., Zhou, M., et al. (2014). Cold electron heating by EMIC waves in the plasmaspheric plume with observations of the Cluster satellite. *Geophysical Research Letters*, *41*, 1830–1837. <https://doi.org/10.1002/2014GL059241>
- Zhang, J.-C., Kistler, L. M., Mouikis, C. G., Klecker, B., Sauvaud, J.-A., & Dunlop, M. W. (2011). A statistical study of EMIC wave-associated He^+ energization in the outer magnetosphere: Cluster/CODIF observations. *Journal of Geophysical Research*, *116*, A11201. <https://doi.org/10.1029/2011JA016690>
- Zhang, X.-J., Angelopoulos, V., Artemyev, A. V., Hartinger, M. D., & Bortnik, J. (2020). Modulation of whistler waves by ultra-low-frequency perturbations: The importance of magnetopause location. *Journal of Geophysical Research: Space Physics*, *125*, e2020JA028334. <https://doi.org/10.1029/2020JA028334>
- Zhang, X.-J., Chen, L., Artemyev, A. V., Angelopoulos, V., & Liu, X. (2019). Periodic excitation of chorus and ECH waves modulated by ultralow frequency compressions. *Journal of Geophysical Research: Space Physics*, *124*, 8535–8550. <https://doi.org/10.1029/2019JA027201>
- Zhang, X.-J., Li, W., Thorne, R. M., Angelopoulos, V., Bortnik, J., Kletzing, C. A., et al. (2016). Statistical distribution of EMIC wave spectra: Observations from Van Allen Probes. *Geophysical Research Letters*, *43*, 12348–12355. <https://doi.org/10.1002/2016GL071158>
- Zhang, X.-J., Mourenas, D., Artemyev, A. V., Angelopoulos, V., Kurth, W. S., Kletzing, C. A., & Hospodarsky, G. B. (2020). Rapid frequency variations within intense chorus wave packets. *Geophysical Research Letters*, *47*, e2020GL088853. <https://doi.org/10.1029/2020GL088853>
- Zhang, X.-J., Mourenas, D., Artemyev, A. V., Angelopoulos, V., & Sauvaud, J.-A. (2019). Precipitation of MeV and sub-MeV electrons due to combined effects of EMIC and ULF waves. *Journal of Geophysical Research: Space Physics*, *124*, 7923–7935. <https://doi.org/10.1029/2019JA026566>
- Zhang, Y., Matsumoto, H., & Kojima, H. (1998). Lion roars in the magnetosheath: The Geotail observations. *Journal of Geophysical Research*, *103*(A3), 4615–4626. <https://doi.org/10.1029/97JA02519>
- Zhou, Q., Xiao, F., Yang, C., He, Y., & Tang, L. (2013). Observation and modeling of magnetospheric cold electron heating by electromagnetic ion cyclotron waves. *Journal of Geophysical Research: Space Physics*, *118*, 6907–6914. <https://doi.org/10.1002/2013JA019263>
- Zhu, H., Chen, L., Claudepierre, S. G., & Zheng, L. (2020). Direct evidence of the pitch angle scattering of relativistic electrons induced by EMIC waves. *Geophysical Research Letters*, *47*, e2019GL085637. <https://doi.org/10.1029/2019GL085637>
- Zhu, X., & Kivelson, M. G. (1991). Compressional ULF waves in the outer magnetosphere 1. Statistical study. *Journal of Geophysical Research*, *96*(A11), 19451–19467. <https://doi.org/10.1029/91JA01860>
- Zhu, X., & Kivelson, M. G. (1994). Compressional ULF waves in the outer magnetosphere 2. A case study of Pc 5 type wave activity. *Journal of Geophysical Research*, *99*(A1), 241–252. <https://doi.org/10.1029/93JA02106>